ISSN: 2178-7727

A numerical study of solar air collectors with corrugated absorber plates featuring diverse wave amplitudes and wavelengths

Rajiv Bhattacharjee[a] Suman Debnath[a,b]

[a]Department of Mechanical Engineering, Chandigarh University, Gharuan, Mohali, Punjab, 140413
[b]Department of Aerospace Engineering, Chandigarh University, Gharuan, Mohali, Punjab, 140413

ABSTRACT

The impact of varied surface textures, characterized by differing amplitudes and wavelengths, on heat transfer rates and friction factors of absorber plates in solar air collectors has been investigated via numerical simulations. Novel geometric configurations of corrugated absorber plates were explored, with a thorough assessment of collector performance. Analyses encompassed the influence of key parameters including Reynolds number, wave amplitude, wavelength, relative amplitude, and relative wavelength. Investigations had been conducted across a Reynolds number range from 3.8×10^3 to 18×10^3. Utilizing the ANSYS FLUENT code, a 2-D computational fluid dynamics simulation was executed, choosing the renormalization group (RNG) model from the k-ε model as the best fit. The results from smooth duct scenarios were compared with the effects of all the characteristics that were taken into consideration on the friction factor and heat transfer. Optimal heat transfer rates were observed at a relative amplitude of 0.03 and a relative wavelength of 15, while maximum flow friction factors were noted at a relative amplitude of 0.09 and a relative wavelength of 5. Furthermore, the highest values for thermal enhancement factor, relative amplitude, and relative wavelengths, reaching 1.84, 0.03, and 15, respectively, were identified for a Reynolds number of 12,000.

KEYWORDS: Enrichment of heat transfer; corrugated absorber plate; Friction factor; solar air collector, Thermal enhancement factor.

INTRODUCTION

Solar air collectors (SACs) represent a simple yet highly efficient means of harnessing abundant solar energy for practical thermal applications. Renowned for their uncomplicated design, ease of upkeep, and affordability, SACs have garnered widespread adoption across diverse sectors including space heating, food drying, and timber seasoning [34, 35]. Usually made up of glass coverings [32], an absorber plate, insulation, and a working fluid, home solar-powered air conditioners (SACs) provide a flexible way to use solar energy. Roughening the flow route to improve surface area contact and adding features such as corrugations [8, 23], ribs [1, 3, 5, 6, and 20], and vortex generators [2] are some of the strategies utilized to maximize heat transfer from the absorber plate to the working fluid. These approaches, demonstrated in previous studies, serve to expedite heat transmission and enhance overall collector performance.

The goal of multiple investigations “has been to increase the rate of heat transfer in solar air collectors (SACs) by adding ribs to the absorber plate. In order to examine the friction factor (FF) and heat transmission properties of SACs with forced convection, Bhagoria et al. [1] did experimental studies. According to their findings, in contrast to a smooth duct, the addition of wedge-shaped ribs increased the Nusselt number (Nu) and FF by 2.4 & 5.3 times, correspondingly. In a comparable manner, Bopche et al. [2] investigated the heat transfer properties of SACs on the absorber plate that had U-shaped turbulators. When compared to a smooth duct, the U-shaped turbulators greatly increased the rate of heat transmission, increasing it by 2.82 times for heat transfer and 3.72 times for FF. Multiple v-ribs' impact on a solar air heater's absorber plate was experimentally studied by Hans et al. [3], who also established correlations for Nu and FF. Using w-shaped ribs attached to the absorber plate's bottom, Lanjewar et al. [4] explored the heat transmission and FF properties of SACs and discovered that these values rose by 2.36 & 2.01 times, correspondingly, in comparison to a smooth duct. Karwa and Chitos [5] explored the thermal as well as hydraulic performance of SACs

DOI: 10.57030/ASCI.25.4.AS15

ISSN: 2178-7727

experimentally employing 60˚ v-down ribs on the absorber plate. In" comparison to a smooth duct collector, the experimental research done by Deo et al. [6] using staggered ribs and v-down turbulators showed that the thermal enhancement factor (TEF) and Nu were 2.45 & 3.34 times greater, correspondingly. The effects of right-angle triangular ribs were studied numerically and experimentally by Gawande et al. [7], using normalized pitch and height values of 7.14 & 0.042, correspondingly. They discovered that the thermohydraulic performance outperformed the baseline model by a factor of 2.03.

Skullong et al. [8] carried out the combined impact of delta wing and corrugated-groove vortex generator on solar air heater for uniform heat flux on the wall. The combination of these two gave thermal performance about 37.7-46.3% better than the groove alone, and 1.5-12.5% more efficient than the non-perforated and groove combination. Kumar. [9] experimentally investigated the SAC passage using dimpled multiple V-pattern obstacles. When compared to other obstacle geometry SACs, the thermo-hydraulic performance of V-pattern multiple dimpled obstacles was found to be 7.0 percent greater. Nadda et al. [10] performed experimental research employing arc obstacles on the absorber plate. Optimum outcomes were obtained at a relative width ratio of 5.0, height ratio of 1.0, and pitch ratio of 9.5. The correlations have been formed for $\overline{Nu}$ and FF deviated by ± 9% and ± 11% from experimental results. Kumar et al. [11] providing broken V-pattern baffles, investigated an experimental inquiry to explore the FF and heat transmission properties of a solar air channel. A correlation of $\overline{Nu}$ FF as a function of broken V-pattern baffles was reported. $\overline{Nu}$ and FF was noted to be 4.78 times and 5.64 times greater than the results obtained with smooth duct.

A number of numerical investigations have been done to capture the underlying physics, even though much experimental research has concentrated on "fluid flow characteristics and the optimization of heat transfer. In computational research that looked at the friction factor (FF), performance enhancement, and heat transfer coefficient of solar air collectors (SACs), Kumar and Saini [12] employed arc-shaped ribs to produce artificial roughness, resulting in a maximum overall enhancement ratio of roughly 1.7. To examine heat transfer and fluid flow, Karmare and Tikekar [13] performed a numerical analysis on the absorber plate's bottom surface employing staggered grit ribs (square, round, and triangular). The findings demonstrated that, in comparison to circular and triangular ribs, square ribs offered a 30% higher heat transfer rate at an attack angle of 58˚. Yadav and Bhagoria [14] examined the effects on fluid flow and heat transmission of circular, square, and triangular ribs affixed to the absorber plate using numerical simulations. A parametric analysis of the Reynolds number (Re), roughness pitch (P/e), and relative height (e/D) was part of their investigation. For various values of P/e and e/D, they noted that as Nu increased, FF decreased with an increase in Re. The thermo-hydraulic "performance of staggered multi v-ribs was noted to be 6% better than other rib configurations by Kumar and Kim [15] when they examined the performance of SACs with multi v-ribs on the absorber plate. In a numerical" investigation, Alam and Kim [16] found that, at a 75° attack angle, a semi-ellipse-shaped tabulator improved the performance of a solar air heater to a maximum of 2.05 enhancement ratio. Additionally, Kumar and Kim [17] did a 3-D computational fluid dynamics study of several v-pattern ribs and demonstrated that in comparison to other v-pattern ribs, a v-pattern with grooved ribs offered a greater heat transfer rate. Regarding heat transfer and FF, Kumar et al. and Ammar et al. [18, 34] examined the fluid flow characteristics of a triangular duct with rectangular ribs. They discovered an optimal overall performance factor of 1.89 at Re = 15,000, with e/D, aspect ratio of rib (e/w), and relative roughness rib (P/e) values of 4.0, 10, & 0.04, accordingly. To assess the impact of staggered broken arc ribs on heat transfer rate as well as FF characteristics, Gill et al. [19, 31] did a 3-D numerical analysis of SACs. They discovered that the greatest enhancement occurred at relative pitch, relative height, and normalized rib position values of 10, 0.043, and 0.4, respectively. In two dimensions, Thakur et al.'s study [20] explored the performance of a solar air heater roughened with hyperbolic ribs. At Re = 6000, the maximum enhancement was obtained with a rib pitch of 10mm as well as a rib height of 1mm. The numerical analysis of SACs with sinusoidal absorber plates was investigated by Manjunath et al. and Alio et al. [21, 33], who found a 12.5% increase in thermal efficiency over the base model.

ISSN: 2178-7727

In the development of the solar air collector along with experimental and numerical analyses theoretical ones were also performed by a few researchers. Mohammadi and Sabzpooshani [22] presented a detailed theoretical study of SAC, baffles, and fins attached to the absorber plate. It was demonstrated that the width of the baffles was an important parameter when Re increased in a turbulent flow" regime. However, it was also reported that in order to achieve maximum performance of SAC with an optimum number of fins and baffles, constant mass flow was required. The annual performance was explored under the same weather conditions. It was found that at a temperature of 375°C the power plant improved power by more than 30 MW. The power was efficiently improved by around 45% throughout the year. Sahu and Prasad [23] conducted exergy and thermo-hydraulic performance-based analytical studies to evaluate the overall performance of SAC with absorber plates roughened with arc and circular-shaped ribs, respectively. It had been noted that while an absorber plate with circular-shaped ribs gave 56% better performance than smooth SAC, arc-shaped ribs yielded maximum effective and thermal efficiency of 75.24% and 79.84%, respectively for all investigated parameters. Due to their ease of use as well as low cost, solar air heaters are widely used. They improve performance by employing materials with phase changes and surfaces that have been roughened. Maximizing the use of solar energy through optimal design is made possible by energy and exergy calculations [36].

Because a laminar sub-layer forms between the absorber plate and the moving air, solar air heaters (SAHs) frequently struggle to attain successful convective heat transfer. To solve this, the absorber surface was given artificial roughness. Specifically, one side of the SAH wall was given a unique double arc discrete roughness geometry, while the other sides were covered in insulation. Outdoor testing, conducted under varying roughness parameters, solar radiation intensities, and times of day, revealed that optimal heat transfer and thermal performance were achieved at specific relative roughness pitch and attack angle values, showing significant improvements compared to smooth absorber plates [37]. Given the rising costs of fuel, enhancing the efficiency of SAHs is crucial. A new SAH design with grooved absorber surfaces was analyzed using numerical simulations across a range of Reynolds numbers (3000 to 24000), demonstrating that the grooves induced secondary flows and longitudinal vortices, which enhanced air mixing and convective heat transfer. Multi-objective optimization indicated that larger angles, moderate shape factors, and lower Res were most effective in optimizing energy consumption while boosting heat transfer [38]. Furthermore, a study that compared the heat transfer capabilities of a finned flat plate solar air heater with a traditional flat plate solar air heater in laminar flow conditions discovered that the finned plate greatly increased thermal efficiency as well as heat transfer rates, particularly at low air mass flow rates. This implies that high-performance SAHs with the ability to provide hot air even at low flow rates could be developed [39]. Even though using solar energy has its benefits, SAHs are frequently constrained by low thermal performance because of ineffective heat loss and transfer. The solar air heater's overall efficiency was intended to be improved by expanding the absorber area and improving airflow through the introduction of innovative absorber designs with continuous as well as discontinuous rectangular tubes and V-corrugated fins. The new absorbers significantly improve heat transfer and efficiency, achieving higher heat transfer coefficients and Nusselt numbers compared to plain absorbers. They also reduce heat loss and enhance energy efficiency, despite higher pressure drops. The combined tubular and v-corrugated fin design offers promise for more efficient SAHs and sustainable development [40].

After reviewing existing research on solar air collectors (SACs), it's evident that much focus is placed on enhancing heat transfer through methods like ribs, fins, and turbulators, which increase surface area and turbulence. However, corrugated absorber plates offer similar benefits without relying solely on these features. Despite this potential, there's been limited exploration of corrugated absorber plates in SAC research, particularly regarding their impact on *Nu*, FF, and TEF. This study aims to address these gaps by assessing how wave amplitude, wavelength, relative amplitude, and relative wavelength affect FF and heat transfer, and determining the maximum achievable TEF to optimize dimensions and configurations.

PROBLEM STATEMENT

Corrugated absorber plate ducts with different wavelengths and wave amplitude(a) are considered in the

DOI: 10.57030/ASCI.25.4.AS15

ISSN: 2178-7727

present research. All configurations are in 2-D with an average height of 'H' between the top and the bottom surface of the duct. Three different wave amplitudes (a = 1, 2, and 3 mm) and three different wavelengths (λ = 10, 15, and 20 mm) are chosen i.e. nine different configurations are considered. Three distinct areas comprise the analysis domain: the entry section, the test section, and the exit section. These sections correspond to the air input, the area under investigation, and the air output, respectively. Figure 1 depicts a schematic representation of the physical model.

To make the issue suitable for numerical simulation, the following presumptions are expressed:

- 2D, steady, turbulent, and fully developed are the characteristics of the flow.
- The duct wall and corrugated absorber plate exhibit homogeneity and isotropy.
- Temperature has no effect on the corrugated absorber plates or the duct wall's coefficient of conduction heat transfer.
- Aluminum is employed as the corrugated absorber plate, and air is regarded as the working fluid and incompressible. Table 1 lists the pertinent attributes of these materials.
- We apply a no-slip boundary condition to every surface that comes into contact with the working fluid.
- Losses from radiation and other sources are regarded as insignificant. Radiation loss can be acknowledged as negligible, but heat loss from the collector's wall and cover glass glazing from convection with the surrounding air is crucial.
- The numerical analyses are conducted for Res between 3800 < Re < 18,000 [15].

MATHEMATICAL MODELLING

3.1 Governing equation

The "Navier-Stokes equations and energy equations control the continuity of state and incompressible fluid flow via the roughened duct of a solar air collector with a corrugated absorber panel. The following are the model's governing equations:

Continuity equation:

$$\frac{\partial}{\partial x_i}(\rho u_i)=0 \tag{1}$$

Momentum equation:

$$\frac{\partial}{\partial x_i}(\rho u_j u_i)=-\frac{\partial p}{\partial x_i}+\frac{\partial}{\partial x_j}\left[\mu\left(\frac{\partial u_i}{\partial x_j}+\frac{\partial u_j}{\partial x_i}\right)\right]+\frac{\partial}{\partial x_j}\left(-\rho\overline{u_1'u_j'}\right) \tag{2}$$

Energy equation:

$$\frac{\partial}{\partial x_i}(\rho u_j T)=\frac{\partial}{\partial x_j}\left((\Gamma+\Gamma_t)\frac{\partial T}{\partial x_j}\right) \tag{3}$$

Where and indicate Γ is as molecular thermal diffusivity" and Γ_t is as turbulent thermal diffusivity, respectively.

$$\Gamma=\mu/\mathrm{Pr} \tag{4}$$

$$\Gamma_t=\mu_t/\mathrm{Pr}_t \tag{5}$$

The Eqs. (1) - (2) are known as the Reynolds average Navier Strokes (RANS) equations. The terms $-\rho\overline{u_1'u_j'}$ in Eq.(2) cause the turbulent effect. The Reynolds stresses, $-\rho\overline{u_1'u_j'}$ are modeled through Boussinesq hypothesis in terms of velocity gradients:

$$-\rho\overline{u_1'u_j'}=\mu_t\left(\frac{\partial u_i}{\partial u_j}+\frac{\partial u_j}{\partial u_i}\right) \tag{6}$$

where μ_t is represented by turbulent viscosity. The Boussinesq hypothesis is used almost in all turbulent

ISSN: 2178-7727

models. This theory has the advantage of little calculation time and expense.

3.2 Boundary conditions
For solving Eqs. (1) – (3), inlet and outlet, absorber plate, and other wall boundary criteria are used:
Turbulent intensity (percent) follows Eq. at the inlet, u=1.9-8.8m/s, v=0m/s, T=300 K. (9).
$P = P_{atm}$ at the outflow and Eq. for Turbulent Intensity (percent) follows (9).
u = v = 0 (no-slip condition) m/s at absorber plate, Q=1000W/m^2 (uniform and constant heat flux). where the x velocity component is represented by u and the y velocity component by v.
u = v = 0 m/s at remaining walls (no-slip scenario) Q = 0 W/m^2 (insulated)

3.3 Resource for Numerical Analysis
ANSYS DESIGN MODELER was used to create the 2-D model, and ANSYS ICEM CFD had been employed to construct the grid. Mesh is created by ansys FLUENT for analysis. Hard Disk – 1TB, Processor – Intel ®CoreTM i5-2400 CPU @ 3.10GHz, RAM – 8.00GB, System Type – Windows 7 Ultimate 64-bit, Graphic Card – Nvidia GeForce GT 710 1 GB are the computational configurations employed.

3.4 Analysis Domain
The two-dimensional analysis domain has been generated for CFD analysis presented in Fig. 1(a). A rectangular horizontal conduit serves as the analytical domain in which an aluminum corrugated absorber plate is used in the place of the top wall and bottom side is considered as the smooth surface. Entrance, test, and departure are the three components that make up the computational domain. The entry part was chosen because it allows for the creation of a fully established flow before entering the analysis domain's test section. The entrance and departure sections of an analysis domain should be ordered, according to ASHRAE Standard 93-2003 of $x_1 = 5\sqrt{WH}$ and $x_2 = 2.5\sqrt{WH}$, respectively [24]. "The absorber plate is composed of aluminum and has a thickness of 1 mm. Corrugated absorber plates have been utilized to create turbulence in the flow" channel with varying wavelengths and amplitudes in order to create artificial roughness. The minimum wave amplitude and wavelength have been used 1mm and 10mm, respectively, so that it can easily break the laminar sublayer. The maximum wave amplitude and wavelength have been chosen 3 mm and 20 mm so that it can neglect the passage blockage effect. Figures 1(b) and 1(c) illustrate a sectional and top view of the corrugated absorber plate, respectively. For the simulation, an even heat flow of 1000w/m^2 is delivered to the corrugated absorber plate. Table 2 displays the parameters of the model design. Table 3 contains a list of the parameters that were used in the simulation along with their numerical values.

3.5 Grid generation
ANSYS ICEM CFD has been employed to prepare the grid generation of the analysis domain. A uniform mesh is generated with a very fine element size which can easily break the laminar sub-layer zone. In the present study grid independence is checked by producing uniform grids in seven steps varying from 1,20,000 to 1,96,000 and the element size varies from 0.46 to 0.31 as shown in Table 4. It has been seen that after 1,92,000 elements, again increasing the grid elements the Nusselts number variation is less than 0.06% and that is taken as the criteria for grid independence. The variation of $\overline{Nu}$ with number of elements of grids is depicted in Fig. 2. The uniform mesh with 1,92,00 number of grid elements with 0.32 mm element size is shown in Fig. 3.

3.6 The model selection and validation
The choice of turbulent model is reliant upon the nature of the flow and on the computational power availability. The selection of turbulence model and its validation are performed by comparing the average $\overline{Nu}$. Standard k–model, Realizable k–model, Renormalization-group "k–model, and shear stress transport k–model with Dittus-Boelter correlation [25] are some of the turbulence models available for solar air collectors.
Dittus – Boelter correlation: $\overline{Nu_s} = 0.023\,\mathrm{Re}^{0.8}\,\mathrm{Pr}^{0.4}$ (7)

ISSN: 2178-7727

Blasius correlation: $f_s = 0.0791\ \mathrm{Re}^{-1/4}$ (8)

Smooth duct FF f_s is represented by Blasius correlation [26].

The comparison of $\overline{Nu}$ a smooth duct is depicted in Figure 4; several turbulence models with Dittus-Boelter correlation are anticipated. The outcomes attained from the Dittus-Boelter correlation and the RNG k–Ɛ model are demonstrated to be in good agreement. This validates the accuracy of the outcomes that the simulation produced. The Dittus-Boelter and RNG k-correlation that was obtained is ± 1.95 deviations. A number of other turbulence models, including the shear stress transport k–Ꝁ model, the realizable k–Ɛ model, the conventional k–Ɛ model, and others, projected outcomes that differed considerably from the Dittus-Boelter correlation findings. Consequently, the RNG k–ε model has been chosen for simulation and heat transfer characteristic prediction in the current numerical analysis. The" comparison of the smooth duct results with Blasius and Dittus-Boelter is displayed in Figs. 5(a) and (b).

3.7 Boundary condition

A 2-D analysis domain is considered for flow through rectangular ducts. The analytical domain is bounded by intake, walls, and outlet in the x-y plane. Air is the operational fluid. The properties of the corrugated absorber plate (aluminum) as well as the working fluid (air) should remain unchanged at average bulk temperature. A fixed pressure injection of $1.013\text{x}10^5$ Pa is made under uniform air velocity intake and outlet pressure conditions. The air temperature in the duct is first predicted to be 300K. Turbulence intensity(I) is applied at the inlet from the following equation [27]:

$$I = 0.16(\mathrm{Re})^{-1/8} \quad (9)$$

3.8 Transport equations "of RNG k–ε model

The turbulence kinetic energy (TKE), 'k,' and the TKE dissipation rate Ɛ, are both calculated using the formulae below for the RNG k-Ɛ turbulence model.

$$\frac{\partial}{\partial x_i}\left(\rho k u_j\right) = \frac{\partial}{\partial x_j}\left(\alpha_k \mu_{eff} \frac{\partial k}{\partial x_j}\right) + G_k - \rho\varepsilon \quad (10)$$

$$\frac{\partial}{\partial x_i}\left(\rho \varepsilon u_j\right) = \frac{\partial}{\partial x_j}\left(\alpha_\varepsilon \mu_{eff} \frac{\partial \varepsilon}{\partial x_j}\right) + C_{1\varepsilon}\frac{\varepsilon}{k}\left(G_k\right) - C_{2\varepsilon}\rho\frac{\varepsilon^2}{k} - R_\varepsilon \quad (11)$$

In the" Eqs. (10) and (11) G_k and μ_{eff} are represented as turbulence kinetic energy and effective turbulence viscosity and $\alpha_k, \alpha_\varepsilon$ these two are known as inverse effective turbulence Prandtl numbers, respectively. G_k and μ_{eff} can be represented as:

$$G_k = -\rho\overline{u_1' u_j'}\frac{\partial u_j}{\partial x_i} \quad (12)$$

$$\mu_{eff} = \mu + \mu_t \quad (13)$$

here μ_t is known as turbulence viscosity and calculated as a function of k and ε as given below:

$$\mu_t = \rho C_\mu \frac{k^2}{\varepsilon} \quad (14)$$

here C_μ is a constant.

The constants for the turbulence model $\alpha_k, \alpha_\varepsilon, C_{1\varepsilon}, C_{2\varepsilon}$ and C_μ are carried their default values [28]: α_k = 1.39, α_ε = 1.39, $C_{1\varepsilon}$ = 1.42, $C_{2\varepsilon}$ = 1.68 and C_μ = 0.0845.

3.9 Methods for Solution

In this 2-D simulation, the momentum, as well as energy equations, have been solved employing the following techniques: The "gradient-least squares cell-based, momentum-second order upwind, pressure-standard, turbulent kinetic energy energy-second order upwind, and turbulent dilapidation rate-first order upwind in

DOI: 10.57030/ASCI.25.4.AS15

ISSN: 2178-7727

pressure-velocity coupling algorithms are all part of the SIMPLE (semi-implicit technique for pressure linked equations) algorithm [29]. To solve the continuity equations residual is taken 10^{-3} as the converge criterion, and for momentum as well as energy equations, residual is taken 10^{-6} as the converge criterion. But for k and ε converge criterion is taken as 10^{-5}. The standard initialization is chosen to initialize the calculation from the inlet of the analysis domain. The bottom wall of the test section is regarded as an adiabatic" wall, whereas the upper corrugated absorber plate receives a constant, uniform heat flow. At inlet uniform air velocity and at outlet pressure outlet conditions are applied, respectively.

DATA REDUCTION

The $\overline{Nu}$ flow friction factor and TEF are discussed in the present analysis. To construct an effective system, it is important to assess the thermo-hydraulic performance of solar air collectors. The average $\overline{Nu}$ & FF could be defined as follows:

$$\overline{Nu_r} = {hD}/{k} \tag{15}$$

$$f_r = \frac{\left({\Delta P}/{x_2}\right)D}{2\rho v^2} \tag{16}$$

where the co-efficient of convective heat transfer is denoted by h, ΔP denotes the pressure decrease across the X_2 test portion. It is necessary to design the solar air collector so that the working fluid can gain maximum heat energy from the absorber plate with the lowest pumping power consumption. To determine the solar air collector's total performance, thermal as well as hydraulic performance should be evaluated. Webb and Eckert [30] propose an essential metric to compare the results of roughened and smooth ducts at constant pumping power. The parameter is called the Thermal Enhancement Factor (TEF):

$$TEF = \frac{\left({Nu_r}/{Nu_s}\right)}{\left({f_r}/{f_s}\right)^{1/3}} \tag{17}$$

The TEF confirms that if a value of TEF is greater than unity it means the system (solar air collector) is enhanced in heat transfer and using this parameter one can decide which arrangement gives the best results.

RESULTS AND DISCUSSION

Numerical research has been done to evaluate the effects of the various flow and roughness (Re, relative roughness wave '*λ/a*', relative amplitude '*a/D*') configuration of SAC. The corrugated absorber plate's heat transmission and FF properties are addressed. The impacts of roughness and FF parameters are shown after the features of average heat transfer as well as flow friction factor are explored. Under similar operating conditions, the results of corrugated absorber plate and smooth duct are compared for all investigated parameters.

4.1 Validation and test of grid independence

The grid independence test had been used to explore the impacts of artificial roughness on heat transport and FF, as well as to anticipate excellent outcomes. In this simulation, seven sets of grids with various element sizes have been considered for grid independence. The number of elements of grids has been varied from 1,20,000 to 1,96,000 in seven steps. A configuration of a corrugated absorber plate with a Re of 12000 and a wavelength of 15mm, with a wave amplitude of 1mm, was employed to conduct the grid independence test. Fig. 2. reveals variation in $\overline{Nu}$ with number of grid elements. Table 4 shows that the percentage deviation of the average decreases to less than 0.06% when the number of grid elements increases above 1,92,000 elements.

DOI: 10.57030/ASCI.25.4.AS15

ISSN: 2178-7727

For the duration of the simulation, 1,92,000 elements have been selected. The number of elements, size of the elements, and the average $\overline{Nu}$ and percentage deviation of the average $\overline{Nu}$ for the corrugated absorber duct with "the RNG k-ε model are presented in Table 4. To test the validation of the current numerical study, a series of simulations have been performed for smooth ducts with Re ranging between 3800 and 18000. The results of the smooth duct for average FF and $\overline{Nu}$ are depicted in Figs. 5 (a and b). Furthermore, as shown in Fig. 5, the FF values accord well with the Blasius empirical equation 5(a). As shown in Fig. 5, the obtained findings are in good agreement with the Dittus-Boelter equation correlation in the case of" heat transmission 5(b). Alfarawi et al. experimental data were used to validate the acquired results (2-D numerical domain) [35] for Reynolds number as given in [35] and it shows worthy agreement with numerical results as demonstrated in Fig. 5 (c-d).

4.2 The effects of Re

Figure 6. depicts "the influence of the Re on average $\overline{Nu}$ for various values of relative amplitude (*a/D*) and relative wave length (*λ/a*). It is clear from the figure that average $\overline{Nu}$ rises with elevation in Re because of increase in turbulence intensity. The working fluid's turbulence dissipation rate and turbulence kinetic energy rise the turbulence intensity. The heat transmission process may be seen and depicted using the TKE contour. Figure 7 depicts the turbulent kinetic energy contour. For the simulation, the RNG k-Ɛ model was utilized. As" a result, higher value of k increases the turbulent viscosity $\mu_t = \rho C_\mu \kappa^2 / \varepsilon$, sequentially causes higher heat transfer rate. The intensity of TKE decreases as the flow gets closer to the crest, while it is higher close to the corrugated absorber plate trough. The high TKE zone is observed at just below the trough and start of every crest of the wave, intensity of the turbulence kinetic energy decreases as the flow propagate from inlet to outlet. The turbulent intensity contour plot is shown by Fig. 8. for Re of 12000. High turbulence intensity zone is close to the trough and the region after the trough of the wave. The turbulence intensity gradually decreases from inlet to outlet. Turbulence intensity also decreases as the distance from the corrugated absorber plate increases in vertical downward direction. This phenomenon indicates eddies formation near the absorber plate because of the presence of high shear stress. Fig. 9. depicts the velocity contour at a Re of 12000. The presence of vortices because of the waviness of the absorber plate yields better rate of heat transfer. Fig. 10 reveals the variation of FF with the Re at numerous values of relative amplitude (*a/D*) and relative wave length (*λ/a*). It has been noticed that as Re rises, the FF declines owing to the viscous sub-layer concealment. From the above figure, it can be concluded that an elevation in Re rises $\overline{Nu}$ and decline FF for the fixed value of the relative amplitude (*a/D*) and relative wave length (*λ/a*).

4.3 Effect of wave amplitude (a)

Fig. 11 and 12 show variations "of average $\overline{Nu}$ and FF with Re for numerous geometrical configuration of corrugated absorber plates. values of the wave amplitude. In both the figures, it has been observed that as Re rises, the average $\overline{Nu}$ and FF rise and declines, correspondingly. It is also noticed that the value of the $\overline{Nu}$ is more in the case of corrugated absorber plate than the smooth duct, thereby indicating an enhanced heat transfer rate for the corrugated absorber plate". Fig. 11 also shows that average $\overline{Nu}$ increases with decrease in wave amplitude. Furthermore, presence of wave amplitudes causes an increase in turbulence intensity and vorticity. This in turn breaks the suppressed sub-layer and leads to reduction of heat transfer resistance and enhancement of heat transfer rate. So, turbulence should occur near the absorber plate, so that it can easily break the sub-layer of laminar zone.

From Fig. 12, it can be noted that FF rises as the wave amplitude due to the resistance to flow path by corrugated absorber plate. Hence, SACs with corrugated absorber plates requires more pumping power to overcome the high friction resistance. It can be seen from Table 4 that the starting FF ratios are comparatively lesser than the ending FF ratios. The minimum and maximum amplitude of the corrugated absorber plate has been chosen of 1 mm and 3 mm, respectively, so that turbulence can easily break the laminar sub-layer without

ISSN: 2178-7727

causing much flow obstruction.

4.4 Effect of the absorber wave length (λ)

Figures 13 and 14 demonstrate the average influence of Re and the FF at different values of the absorber wave length while keeping the wave amplitude constant. It has been discovered that the value of the $\overline{Nu}$ is greater in case of corrugated absorber plate than the smooth duct, thereby indicating enhanced heat transfer rate for the corrugated absorber plate. From the Fig. 13, it could be noted that at lower values of the Re, wave length has a very negligible effect $\overline{Nu}$. However, as Re increases, $\overline{Nu}$ may increase or decrease with increase in wave length. It can be noticed from Fig. 14 that as wave length rises, FF declines. However, the impact of wave length is relatively more at higher Re.

4.5 The influence of relative wave length (λ/a)

Figs. 15 and 16 show "variation of $\overline{Nu}$ with Re for various values of relative wave length i.e., the combined effect of the wave length and wave amplitude of corrugated absorber plate on flow friction and heat transfer. Fig. 15 (a, b, and c) depicts that as Re increases" $\overline{Nu}$ also increases for all three cases. It has been also noted that heat transfer in case of corrugated absorber duct is higher than smooth duct for all various values of relative wave length. It has been found that the corrugated absorber duct with relative wave length λ/a = 15 and relative amplitude a/D = 0.03 provides maximum $\overline{Nu}$ whereas lowest $\overline{Nu}$ is recorded at relative roughened wave length λ/a = 3.33 and relative amplitude a/D = 0.09 given the whole range of criteria under investigation. The fluctuation as a function of relative wave length is revealed in Figure 16 (a, b, and c). (λ/a) for six different Re at (a) a/D = 0.03, (b) a/D = 0.06, and (c) a/D = 0.09. In every cases, $\overline{Nu}$ rises with rise in Re. At lower values of relative amplitude (a/D = 0.03), change in relative wave length causes minor change in $\overline{Nu}$. However, as relative elevation increases (a/D =0.06, 0.09) $\overline{Nu}$ increases with increase in relative wave length till a critical point, beyond which it becomes asymptotically insensitive to any further change in relative wavelength. Fig. 17 and 18 show the influence of the relative wave length (λ/a) on flow friction factor for range of investigated Re. For a given value of a/D, it can be observed in Fig. 17 (a, b, & c) that as Re increases, the flow friction factor declines. With a lower relative amplitude (a/D = 0.03), FF diminishes as the relative wavelength increases. However, at higher value of relative amplitude, FF may increase or decrease with relative wavelength, depending upon other flow conditions. Fig. 18 (a, b, and c) shows FF as independent and relative wave length (λ/a) as the dependent variable for range of Re at different values of relative amplitude (a) a/D = 0.03, (b) a/D = 0.06, and (c) a/D = 0.09. It has been observed that for a fixed value of relative amplitude, flow FF goes down as a rise in relative wave length (λ/a) and Re. Figs 15 and 16 also shows that as a/D increases, FF also increases for the entire range relative roughness wavelength and Re.

4.6 Effect of relative amplitude (a/D)

Figure 19 depicts the fluctuation of $\overline{Nu}$ with Re at various relative amplitude levels. An increase in relative amplitude causes decrease "in $\overline{Nu}$ for the entire range of Re. So for the present analysis maximum $\overline{Nu}$ is obtained at lower a/D = 0.03. Figure 20 depicts the fluctuation of $\overline{Nu}$ as function of relative amplitude (a/D) for various values of Re, with the relative wave length held constant at /a =15. Similar to relative amplitude, an increase in relative amplitude also causes a decrease in $\overline{Nu}$ for the entire range of Re. It has been observed that as the Re increases $\overline{Nu}$ also increases as it is expected for all relative amplitude.

4.7 Thermal enhancement factor (TEF)

According to an examination of heat transfer and FF behavior of the roughened duct surface, the rate of heat transfer and FF increases as the roughness of the duct increases. The present numerical study shows that the maximum average $\overline{Nu}$ ratio for roughened duct with corrugated absorber plate has been recorded at Re of

DOI: 10.57030/ASCI.25.4.AS15

ISSN: 2178-7727

12000, relative amplitude (*a/D*) of 0.03 and relative wave length (*λ/a*) of 15. Value of the maximum average $\overline{Nu}$ ratio is approximately 1.99 times higher than the $\overline{Nu}$ obtained from smooth duct. On the other hand, roughened duct of relative amplitude (*a/D*) of 0.09 and relative wave length (*λ/a*) of 5 generates the maximum FF which is 2.41 times of FF produced by smooth duct at the Re of 12000. Therefore, it is necessary to select a roughened geometry that yields better heat transfer with relatively lower FF. Equation (16) defines the TEF, a measure suggested by Webb and Eckert [33] that has been employed to assess the thermal as well as hydraulic performance. When TEF is higher than unity, it indicates a system with lower FF and improved heat transport. Figure 21 displays the TEF variation as a function of Re for a range of relative wave" length (/a) and relative amplitude (a/D) values. For every parameter that was looked into, the magnitude of TEF was found to vary between 1.08 to 1.84. The corrugated absorber plate gives maximum value of TEF of 1.84 at *a* = 1 mm, *λ* = 15 mm (i.e. *a/D* = 0.03, *λ/a* = 15) and Re of 12000. In Table 5, you can see the heat transfer enhancement ratio.

4.8 Entropy generation

The variation in entropy generation is illustrated in Figs. 22(a) and 22(b). Specifically, Fig. 22(a) depicts the variation of frictional entropy generation with Re, while Fig. 22(b) reveals the variation in heat entropy generation as a function of Re. As indicated in Fig. 22(a), frictional entropy production increases with rising Res. Among all the configurations, the wave absorber plate with a = 3 mm, and λ = 20 mm has the maximum friction entropy generation for all considered Re. This happens because of waviness of the absorber plate that creates a circulation of fluid, and it has also affect on the viscous irreversibility. Figure 22 depicts the development of thermal entropy as a function of Re (b). Thermal entropy generation diminishes as the Re rises. It can be shown that absorber plates with a = 3 mm and a = 10 mm generate the most thermal entropy, followed by a = 3 mm and a = 20 mm. Now, it is indication worth that for all Re thermal entropy generation is higher for smooth duct collector except a = 3 mm, λ = 10 mm and 15 mm.

CONCLUSIONS

The present investigation utilised a 2-D numerical analysis to explore the flow friction factor as well as heat transfer characteristics of a rectangular solar air collector with a corrugated absorber panel. The analysis looked at the effects of Re, wavelength (λ), relative amplitude (a/D), wave amplitude (a), and relative wavelength (λ/a) on the flow friction factor as well as heat transfer. A numerical analysis had been done for the range of Re (3800-18000). The investigation may lead to the following conclusions:

1. The RNG k-η model has shown better predictive performance when compared to other turbulence models. As a result, the present research uses the RNG k-ᷓ model for both smooth duct validation and grid independence verification.
2. The greatest average Nu was noted to be roughly 93 at Re = 18,000 for a relative wavelength of 15 and a relative amplitude of 0.03. In these circumstances, the maximum increase in heat transfer had been noted to be 1.99 times more than that of the smooth duct.
3. The flow friction factor falls as the Re rises. The maximum flow friction factor measured at a Re of 3800 is 0.0386, which translates to a relative wavelength of 5 and a relative amplitude of 0.09.
4. It has been shown that the largest TEF for the range of parameters tested is given by the corrugated absorber plate, with relative wave length λ/a = 15 and a/D = 0.03. Therefore, heat transfer increase can be achieved with this setup.
5. The rate of entropy creation owing to heat losses is the most important contribution in these types of devices, accounting for maximum of the total rate. This is where researchers should be focused.
6. The overall performance is measured by a factor called TEF whose maximum value is found to be 1.84.

ISSN: 2178-7727

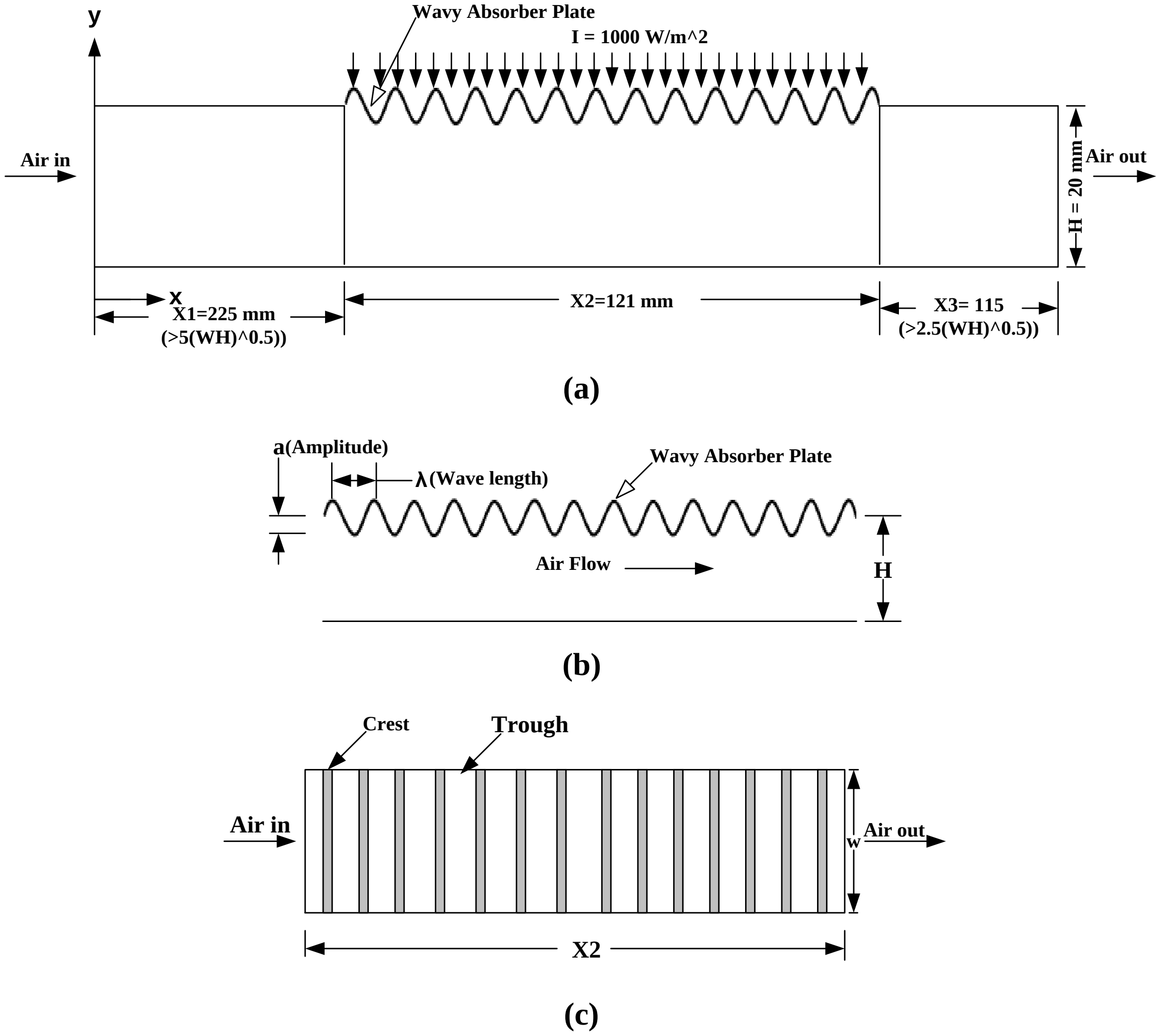

Fig. 1. (a) Schematic diagram (b) Sectional view and (c) Top view of the wavy absorber plate.

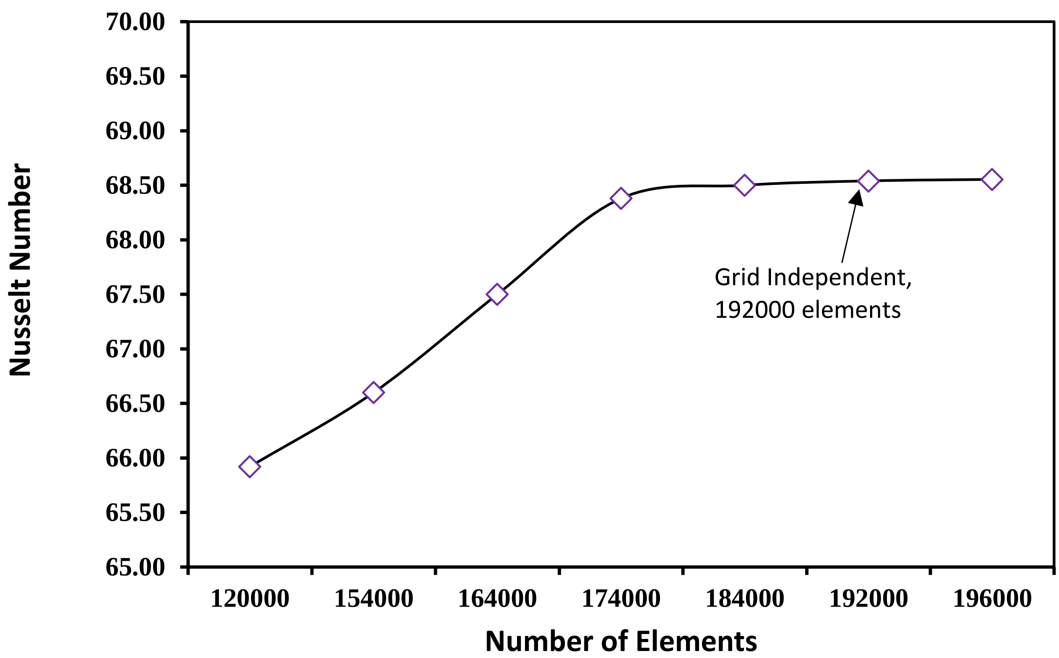

DOI: 10.57030/ASCI.25.4.AS15

ISSN: 2178-7727

Fig. 2. The Nusselt number varies depending on the number of grid elements used in the analysis.

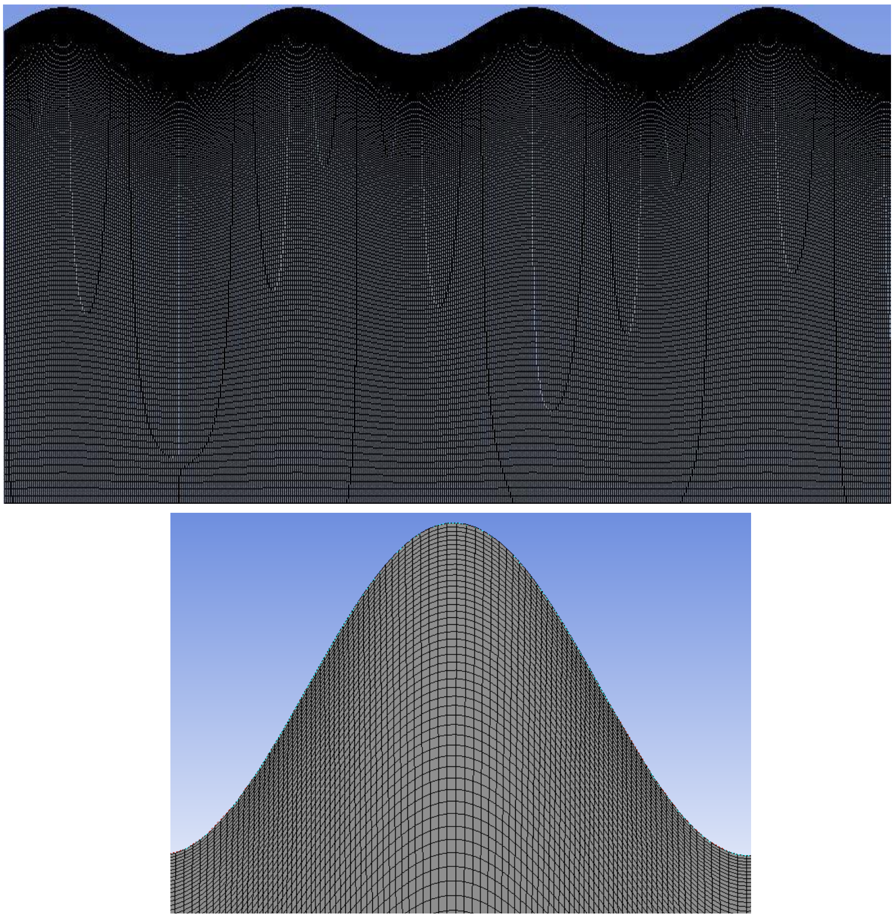

Fig. 3. The computational 2-D mesh at element size 0.32 mm with 1,92,000 number of elements.

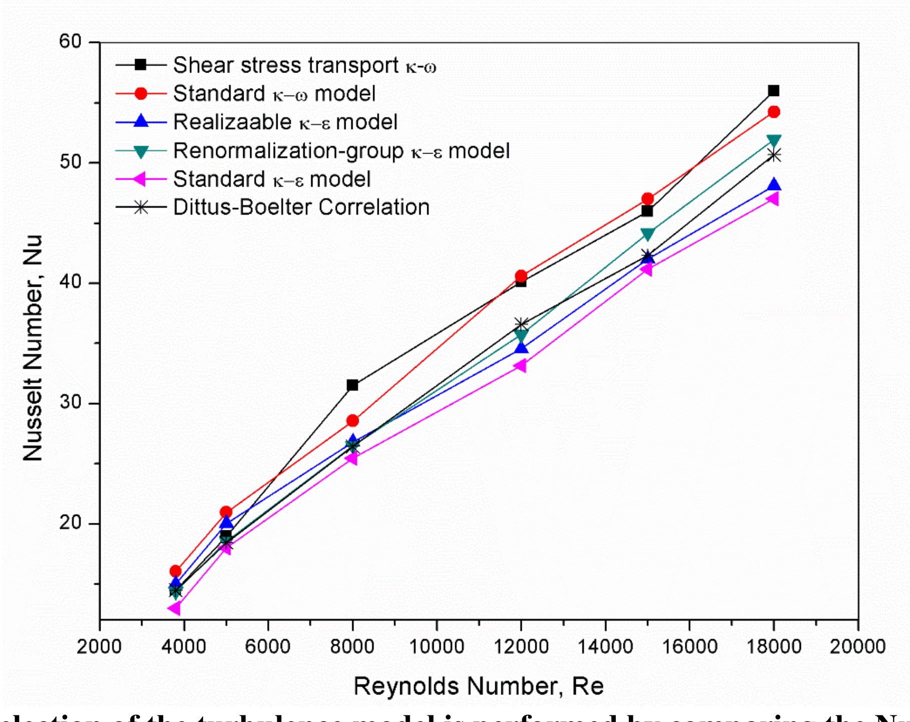

Fig.4. The "selection of the turbulence model is performed by comparing the Nusselt number

ISSN: 2178-7727

predicted by various turbulence models with the Nusselt number calculated using the Dittus-Boelter" correlation for a smooth duct.

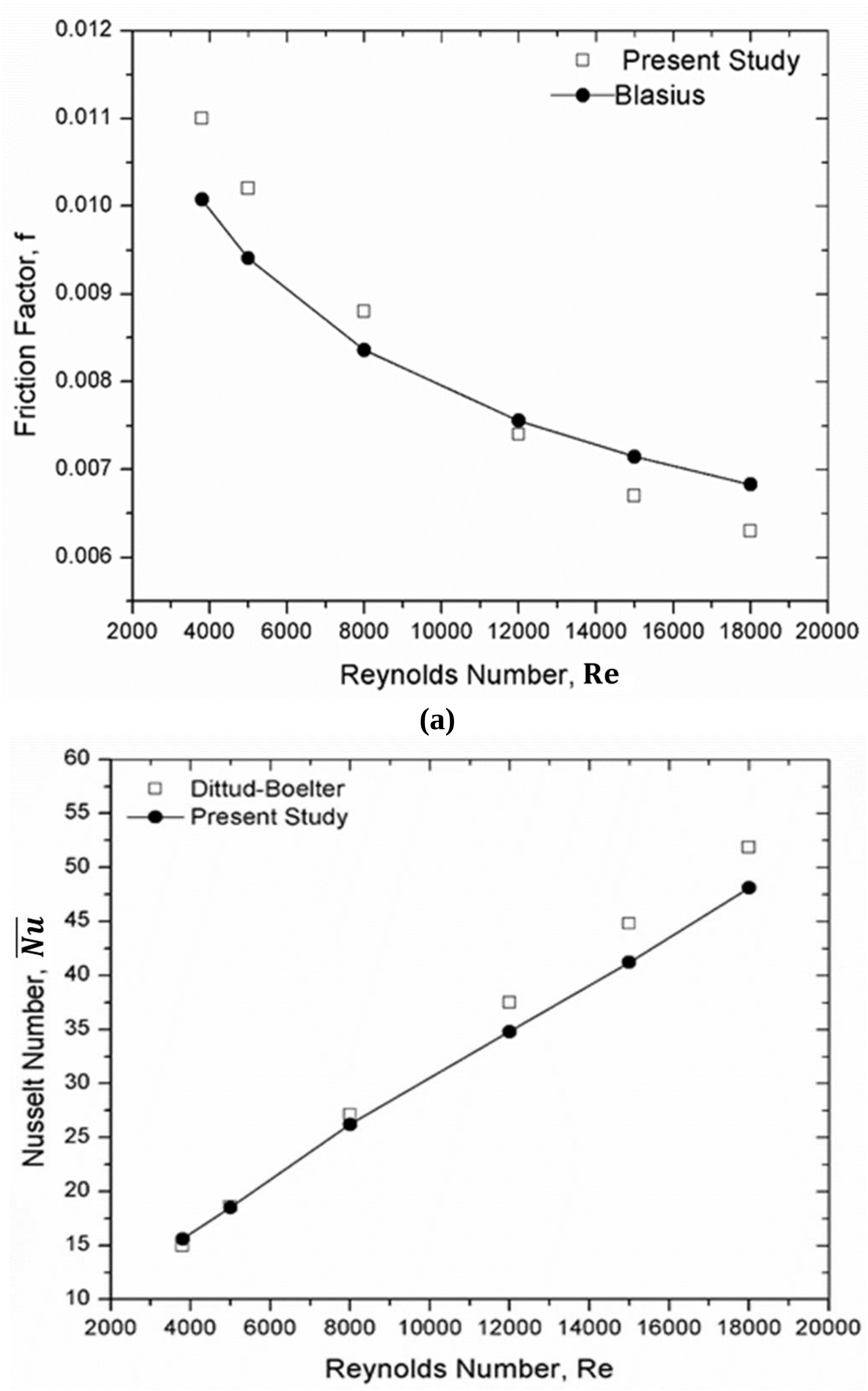

(a)

(b)

ISSN: 2178-7727

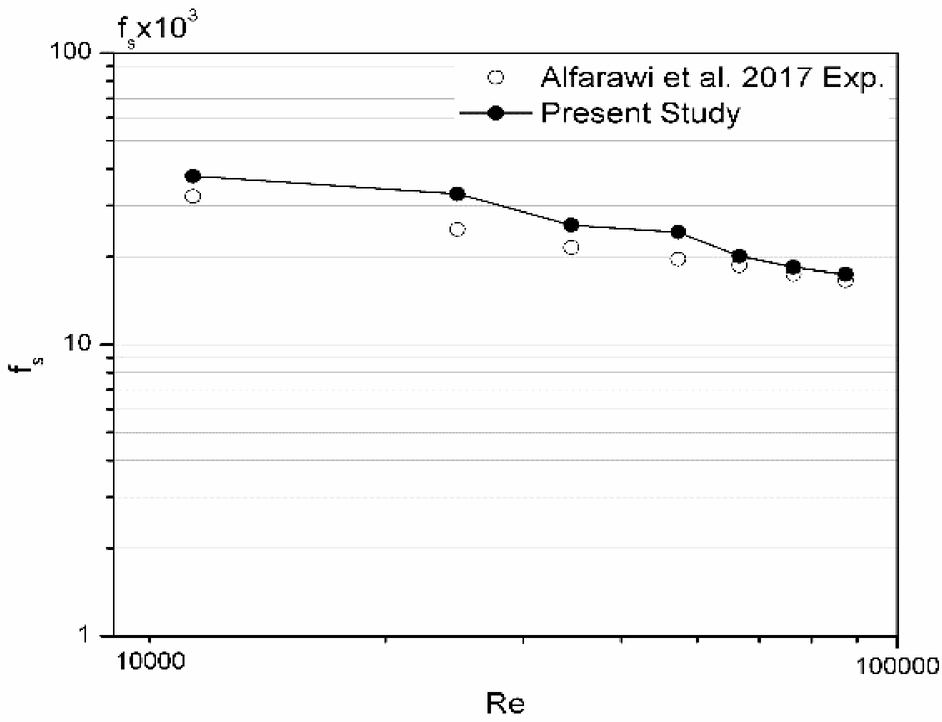

(c)

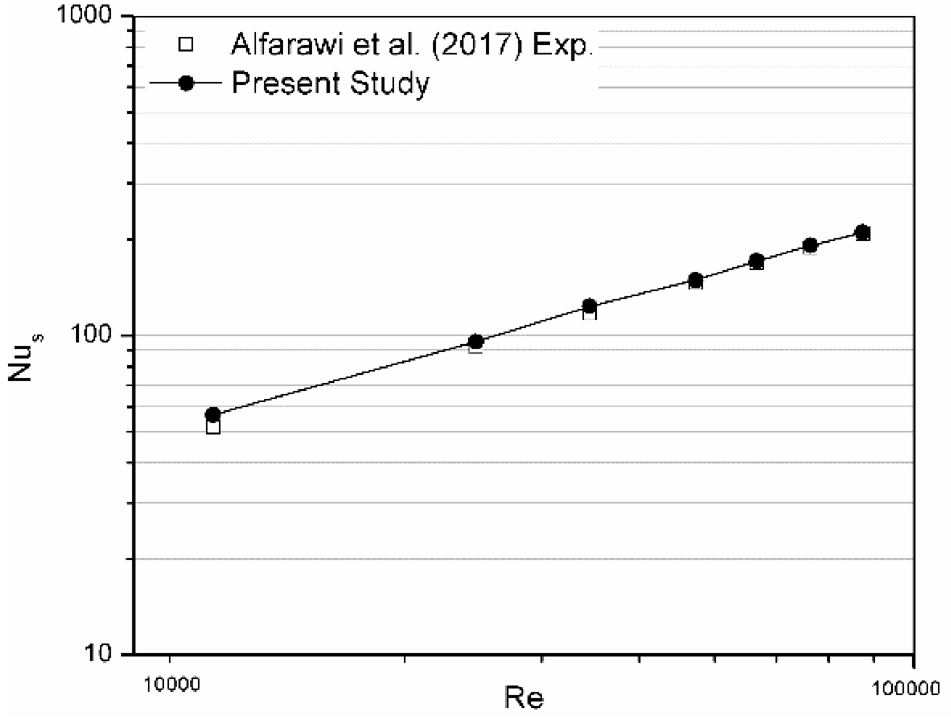

(d)

Fig. 5. The comparison of smooth duct results is illustrated, showing (a and c) the friction factor and (b and d) the Nusselt number against the Blasius and Dittus-Boelter correlations as well as experimental results.

ISSN: 2178-7727

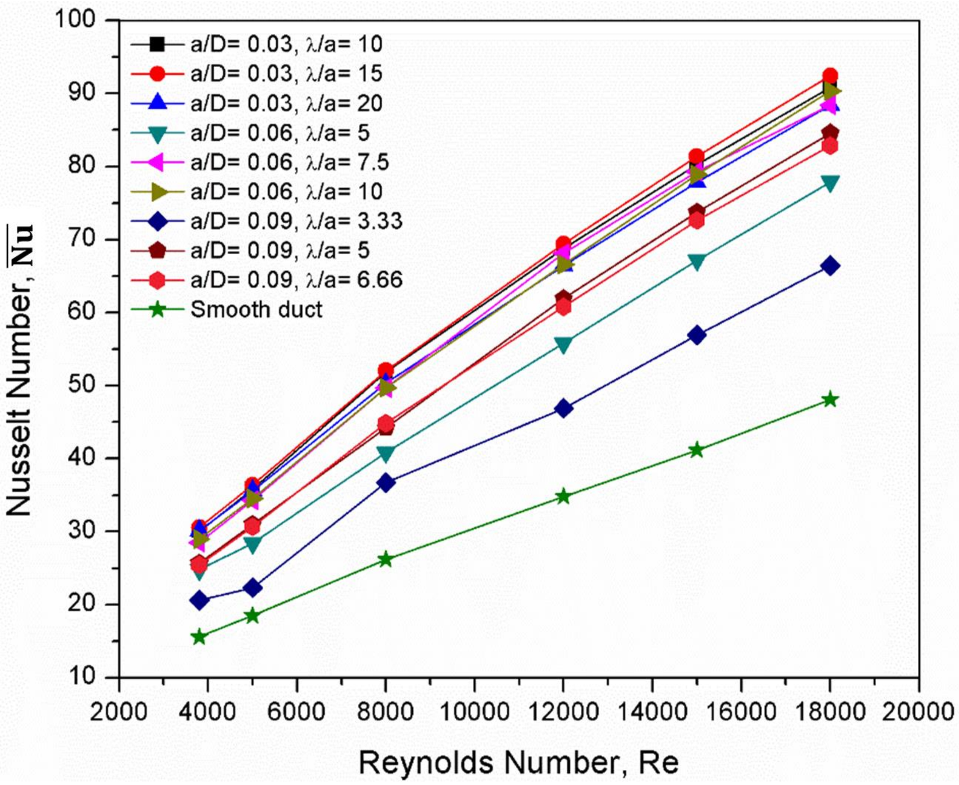

Fig. 6. The variation of the Nusselt number with Reynolds number is presented for different values of relative amplitude (a/D) and relative wavelength (λ/a).

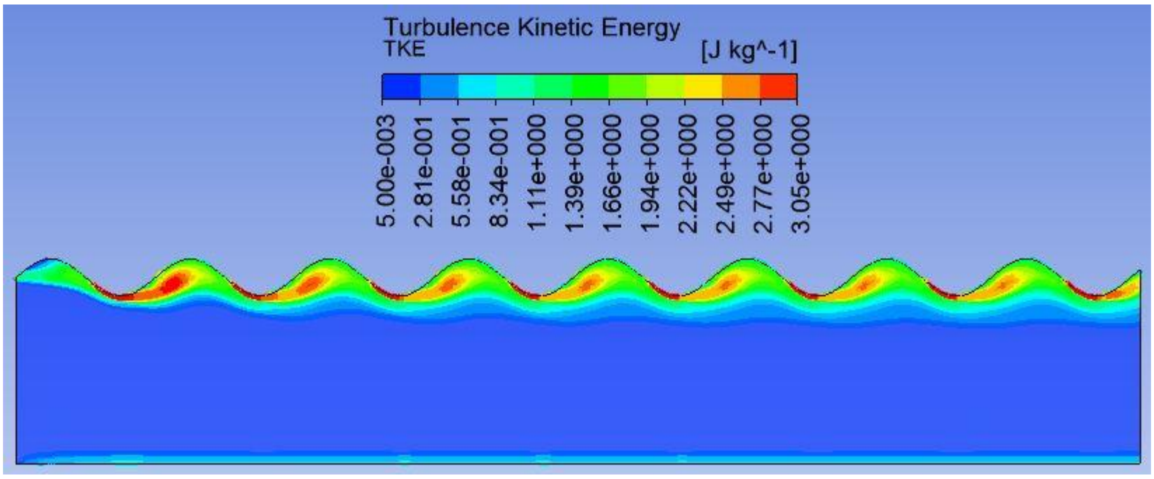

Fig. 7. The Contours of turbulence kinetic energy at a Reynolds number of 12000.

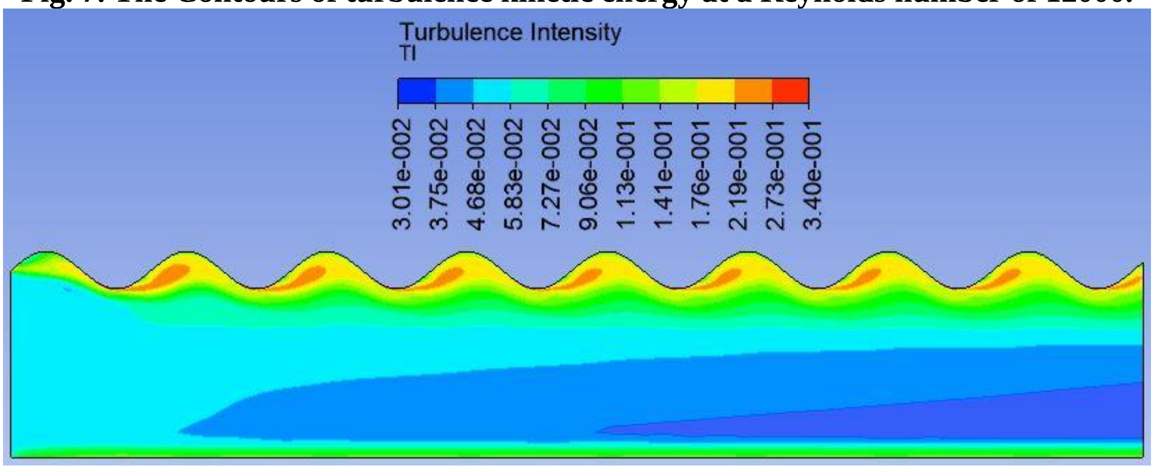

Fig. 8. The Contours plot of turbulence intensity at a Reynolds number of 12000.

DOI: 10.57030/ASCI.25.4.AS15

ISSN: 2178-7727

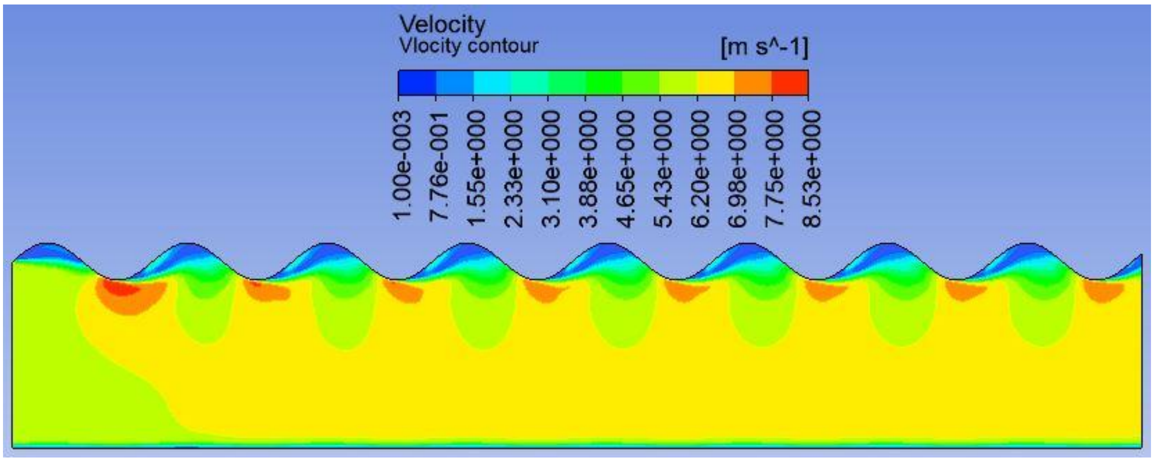

Fig. 9. The velocity magnitude contours at a Reynolds number of 12000.

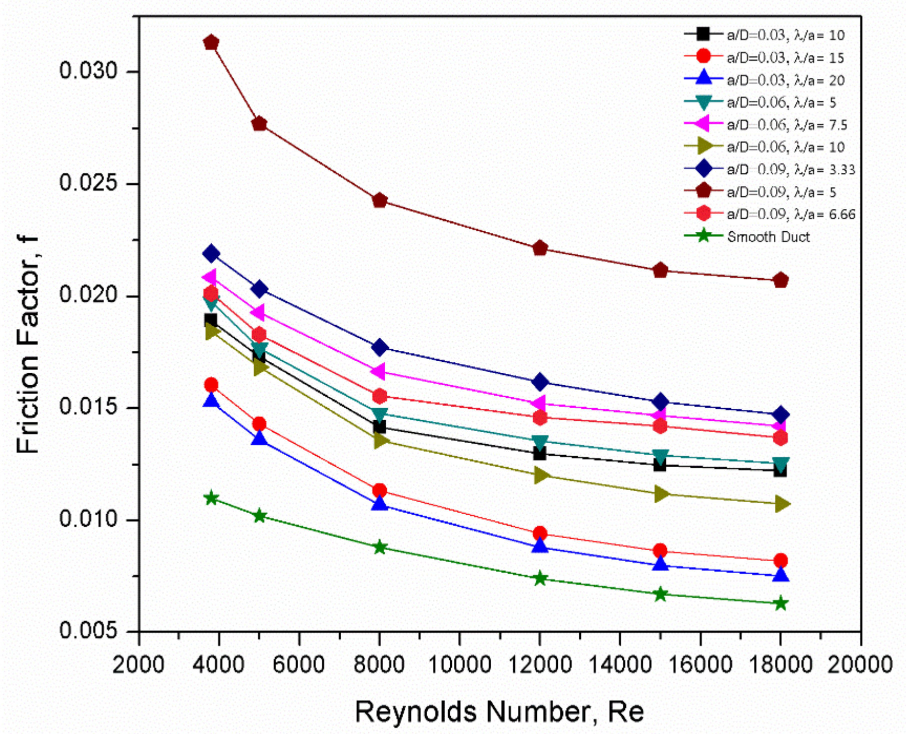

Fig. 10. Variation "of friction factor (f) with Reynolds number (Re) for" various a/D and λ/a.

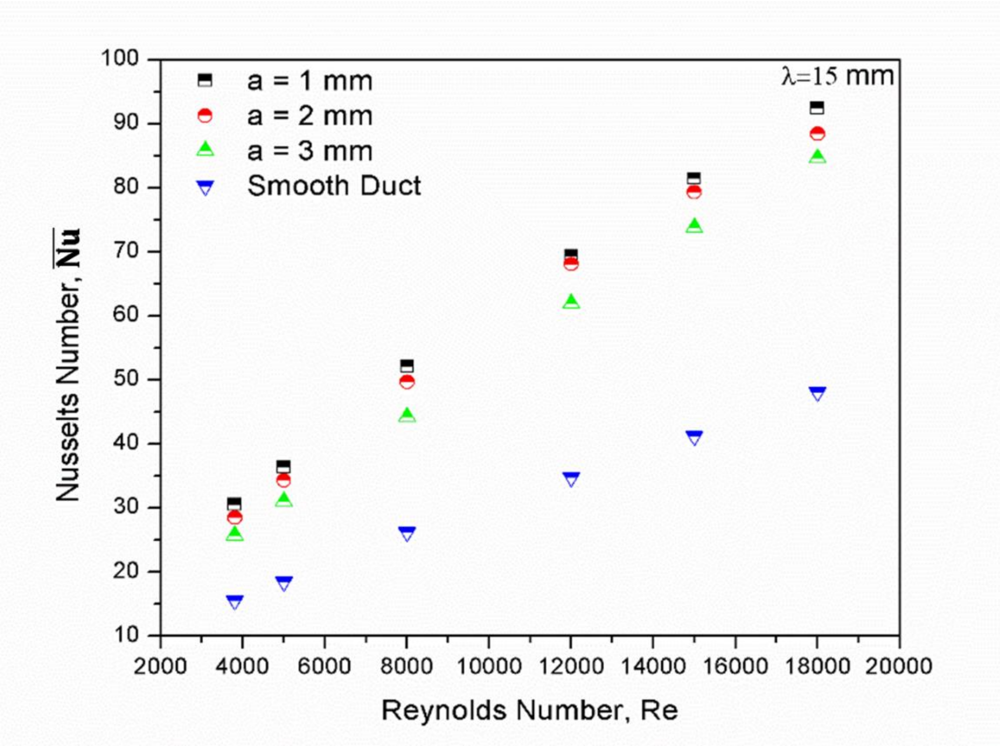

Fig. 11. Variation Nusselt number ($\overline{Nu}$) with Reynolds number for different amplitude of wavy absorber plate, a.

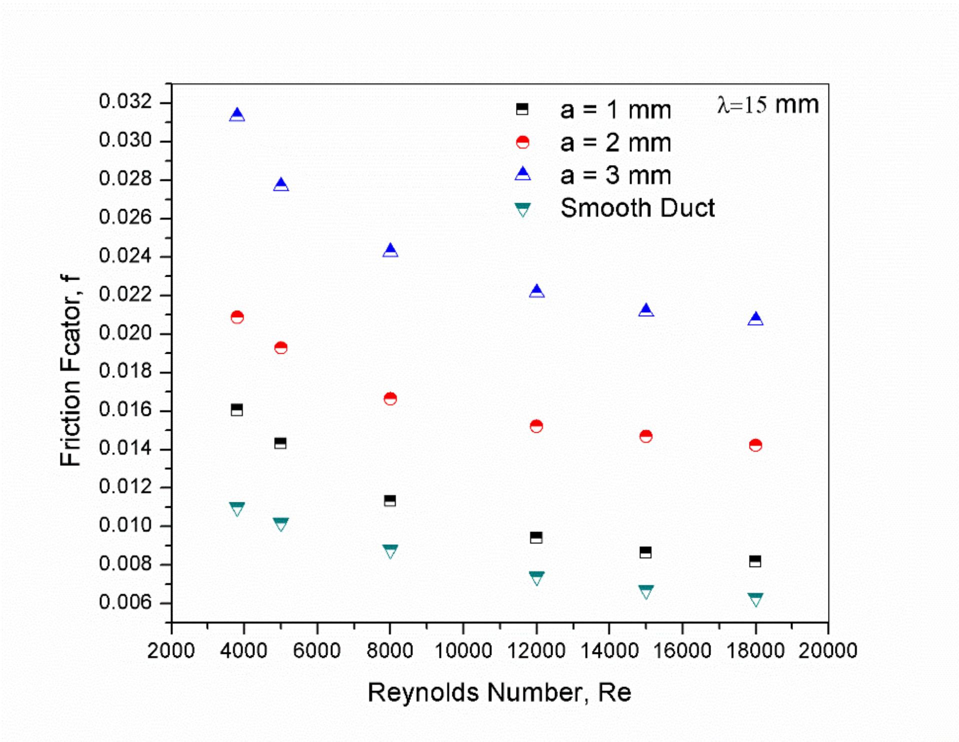

Fig. 12. Variation of friction factor with the Reynolds number for different amplitude of the wavy absorber plate, a.

ISSN: 2178-7727

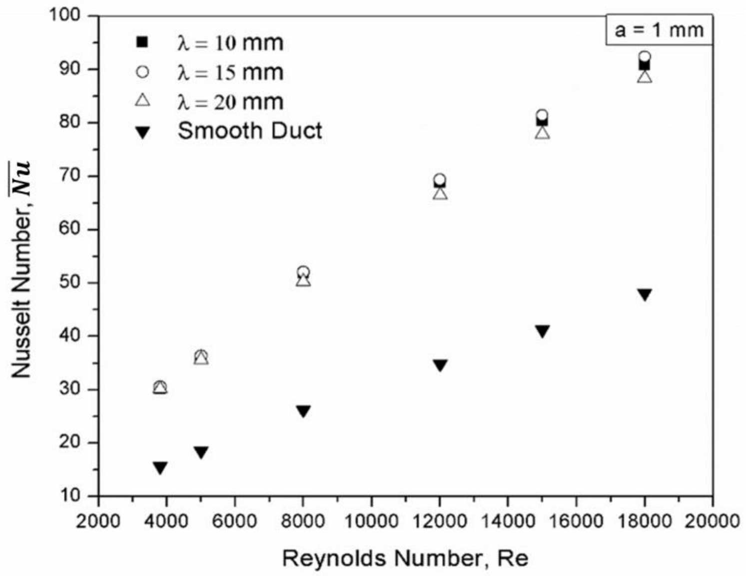

Fig. 13. Variation of the Nusselt number ($\overline{Nu}$)with Reynolds number at various wave length (λ) and fixed amplitude (a).

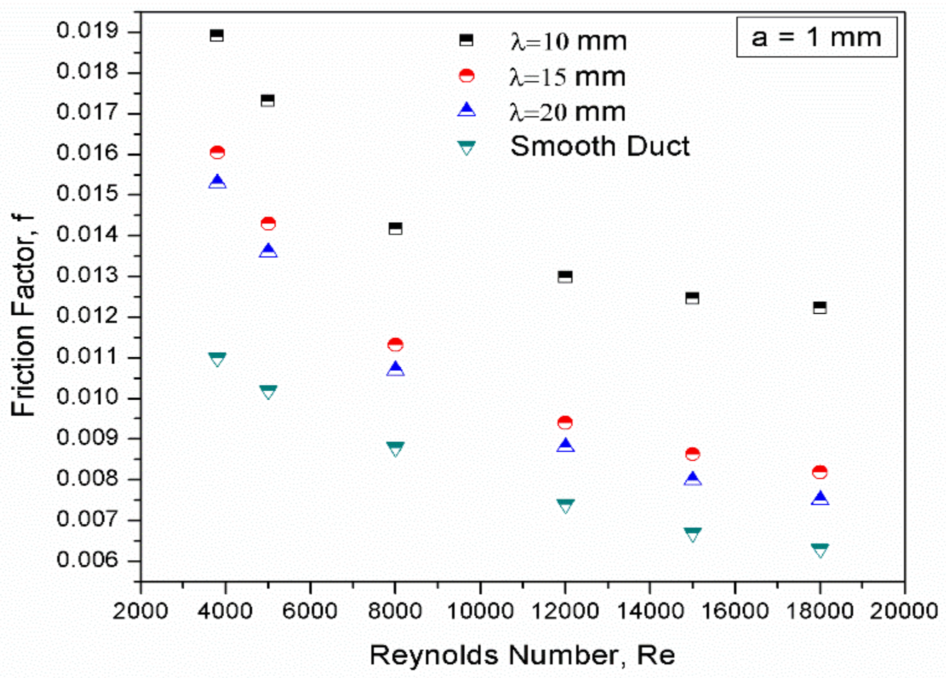

Fig. 14. Variation of the friction factor with Reynolds number at various wavelength (λ) and fixed amplitude (a).

ISSN: 2178-7727

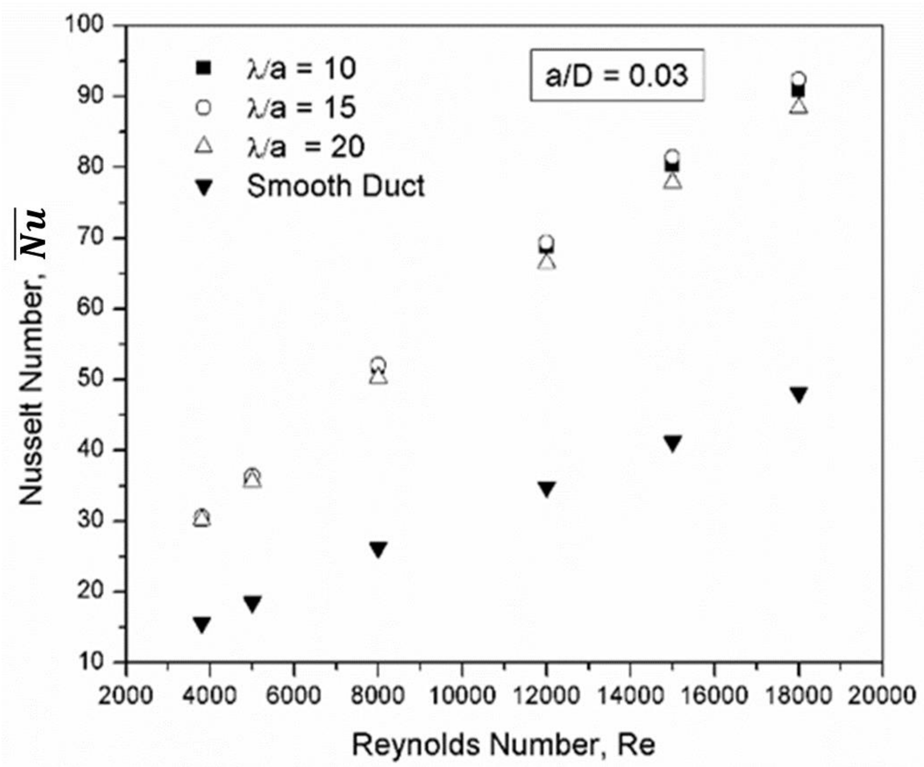

(a)

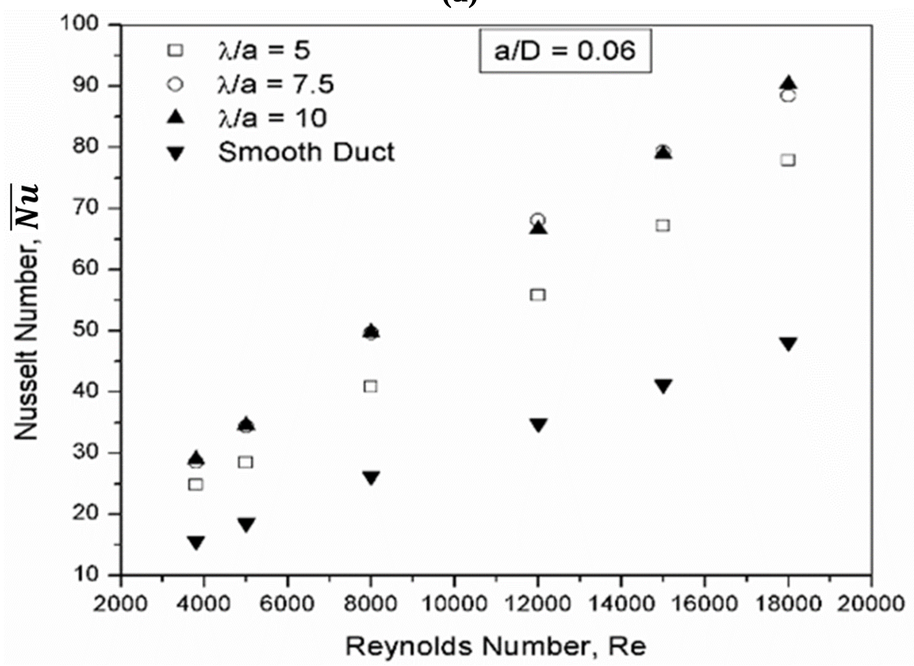

(b)

ISSN: 2178-7727

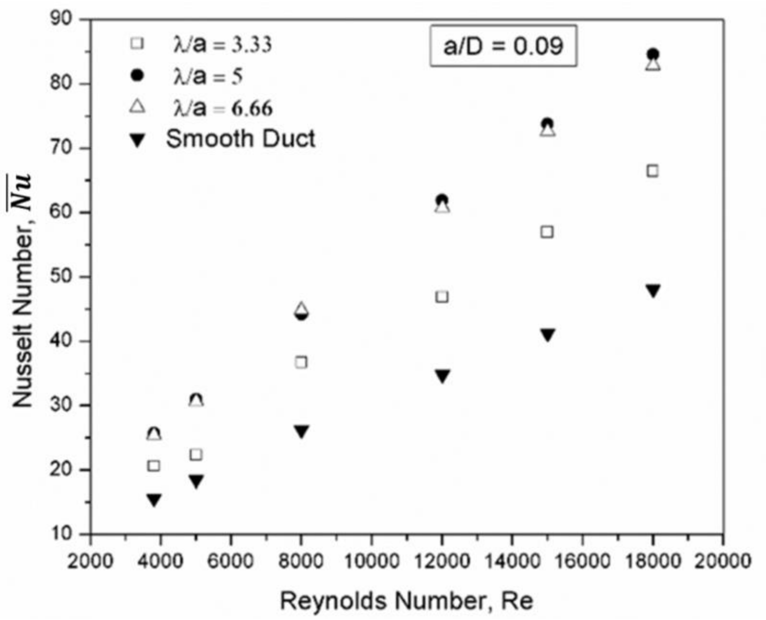

(c)

Fig. 15. Variation of Nusselt number ($\overline{Nu}$) with the Reynolds number for various values of λ/a and for (a) Constant a/D = 0.03, (b) Constant a/D = 0.06, (c) Constant a/D = 0.09.

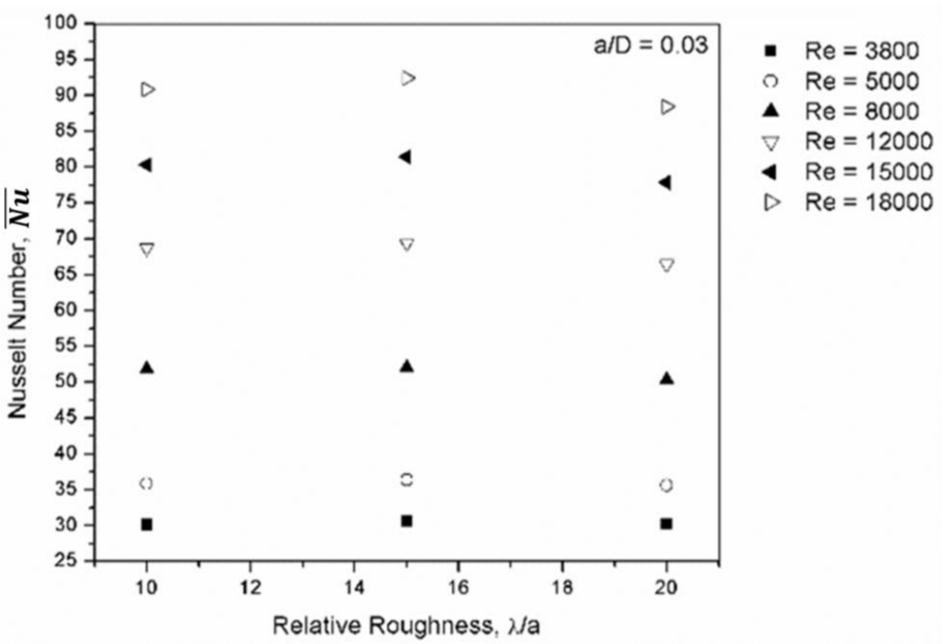

(a)

ISSN: 2178-7727

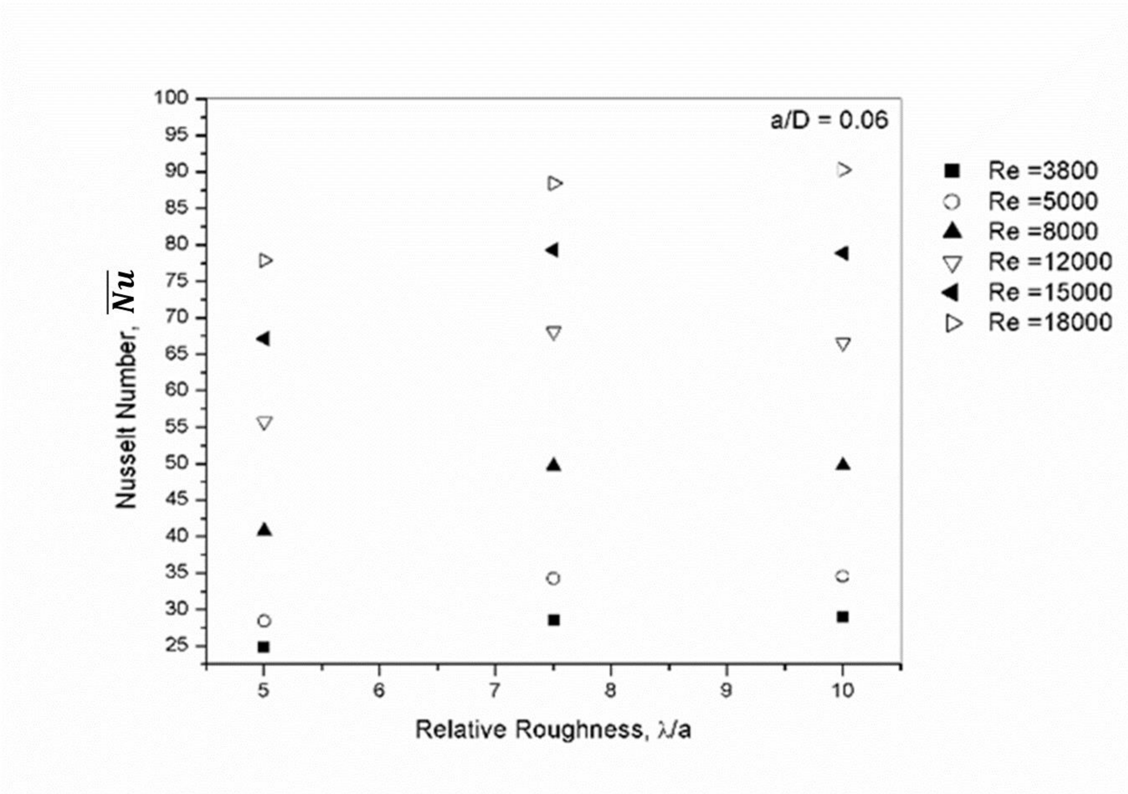

(b)

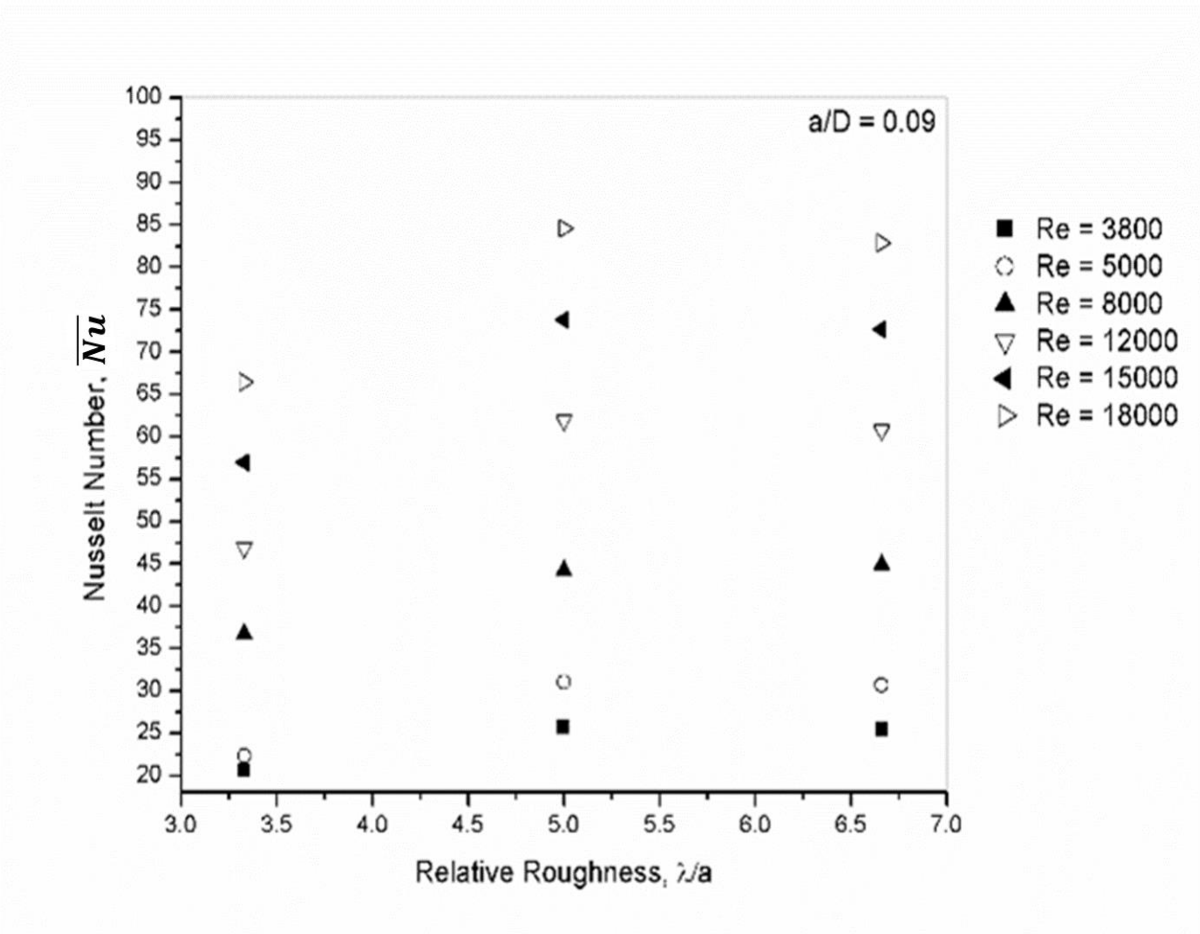

(c)

Fig. 16. Variation of Nusselt number with the relative roughness wave length (λ/a) and for (a) Constant a/D = 0.03, (b) Constant a/D = 0.06, (c) Constant a/D = 0.09.

ISSN: 2178-7727

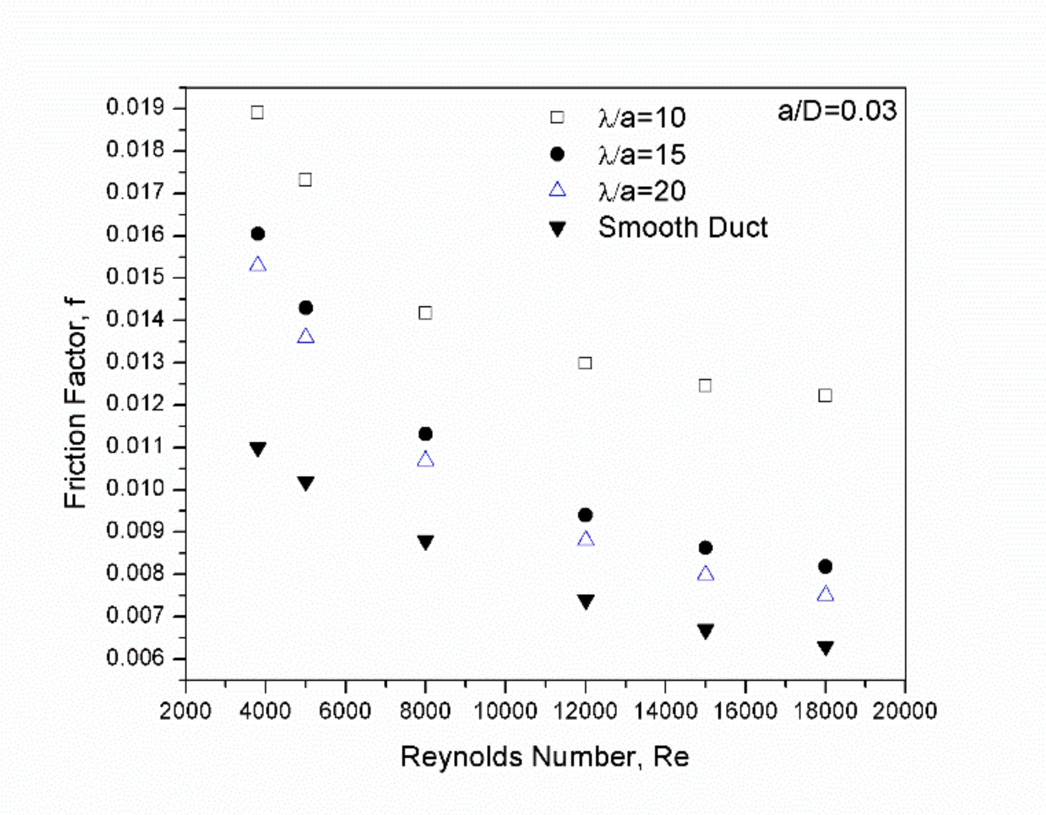

(a)

(b)

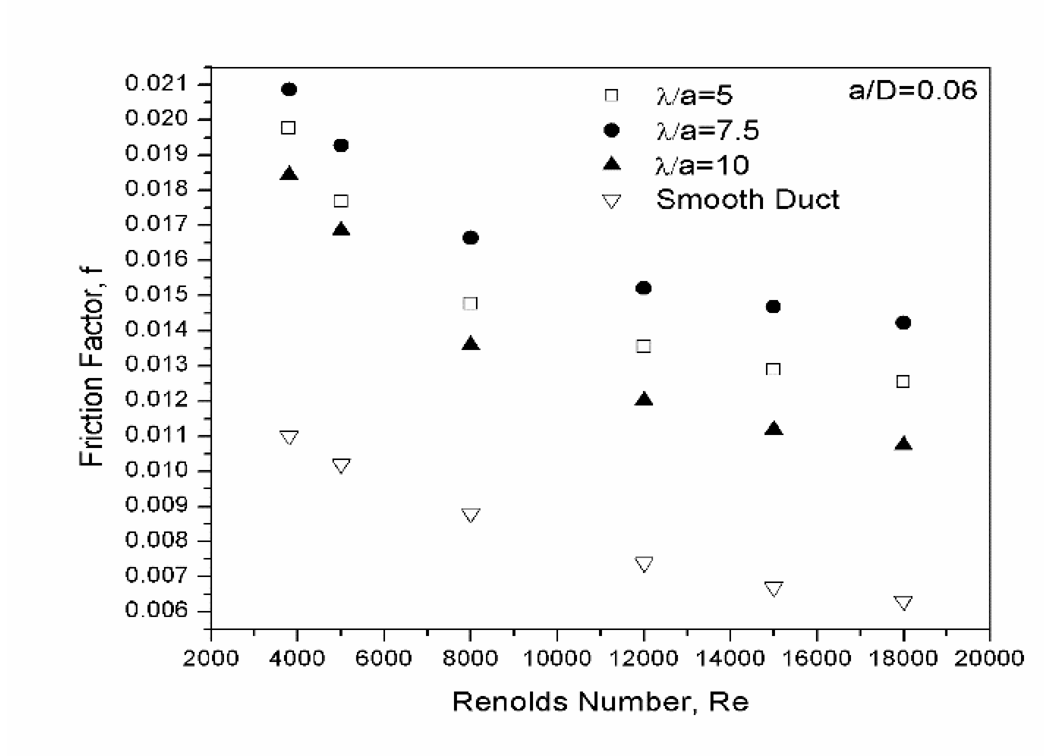

ISSN: 2178-7727

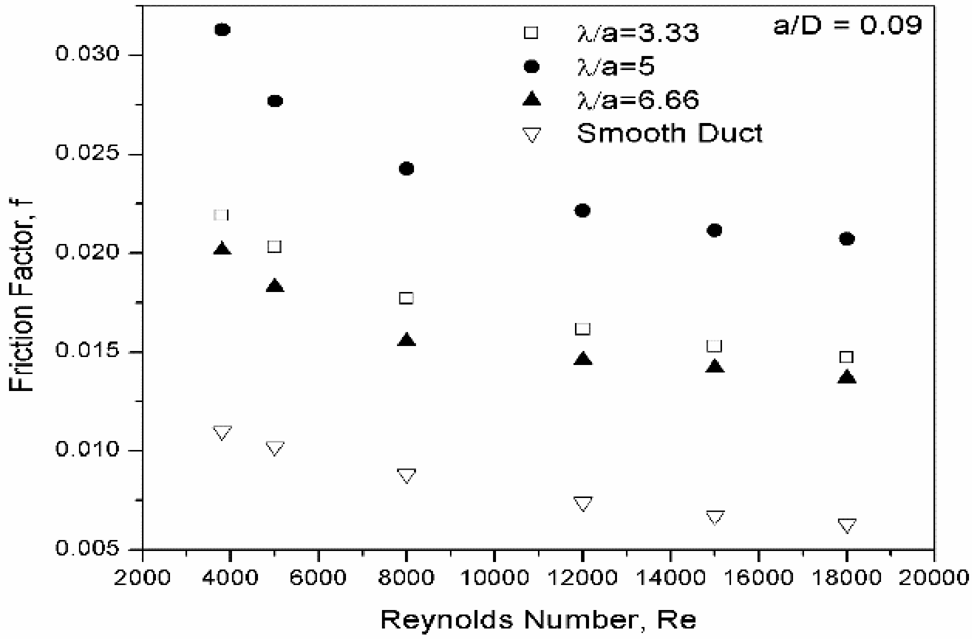

(c)

Fig. 17. “Variation of friction factor as a function of the Reynolds number for the different values of the λ/a, with the (a) Constant a/D = 0.03, (b) Constant a/D = 0.06, and” (c) Constant a/D = 0.09.

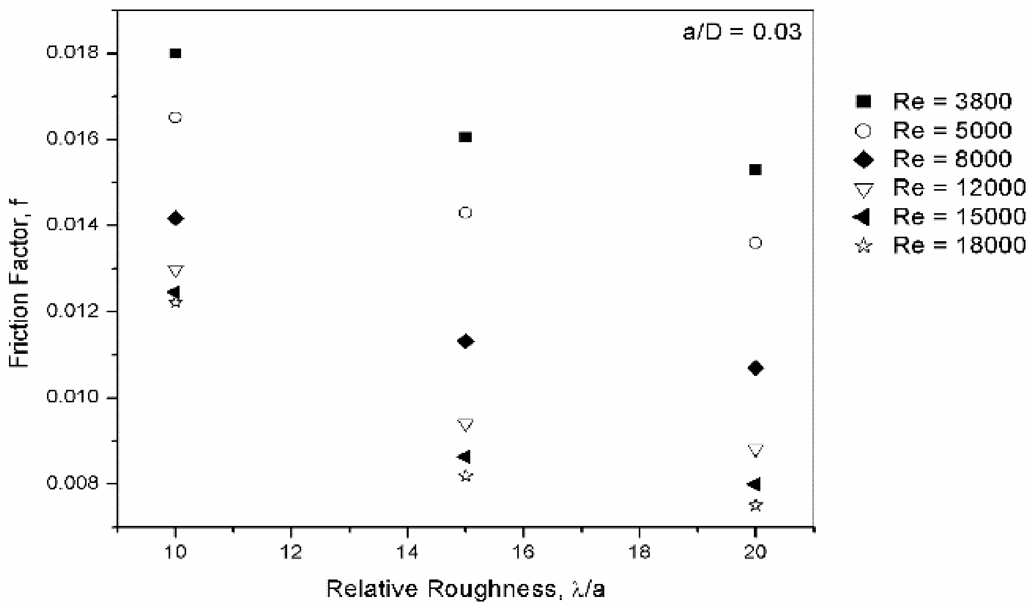

(a)

ISSN: 2178-7727

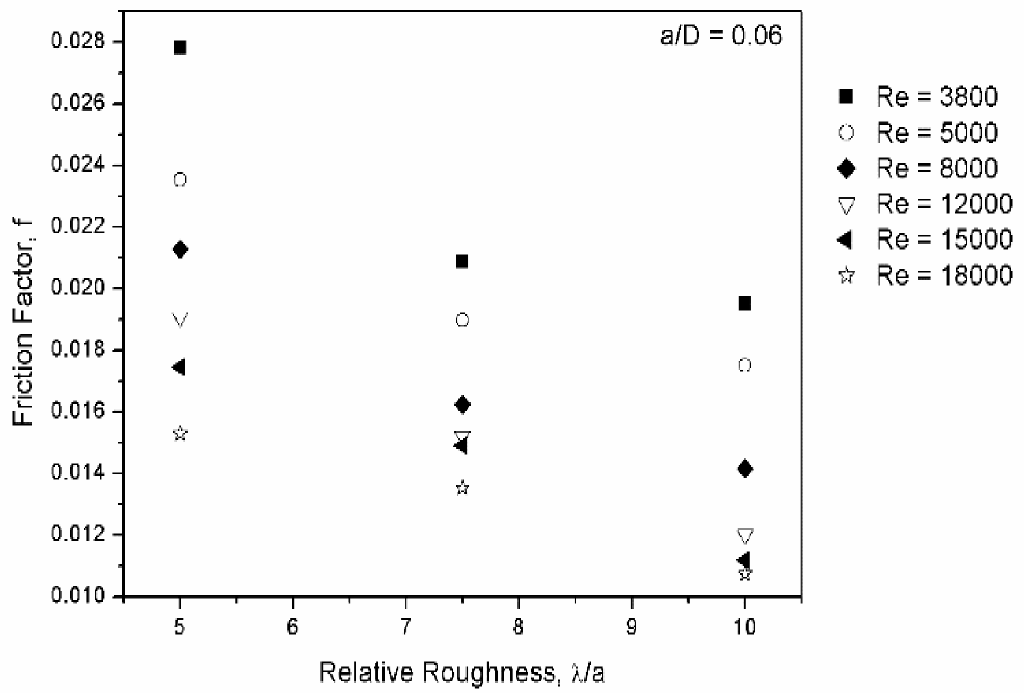

(b)

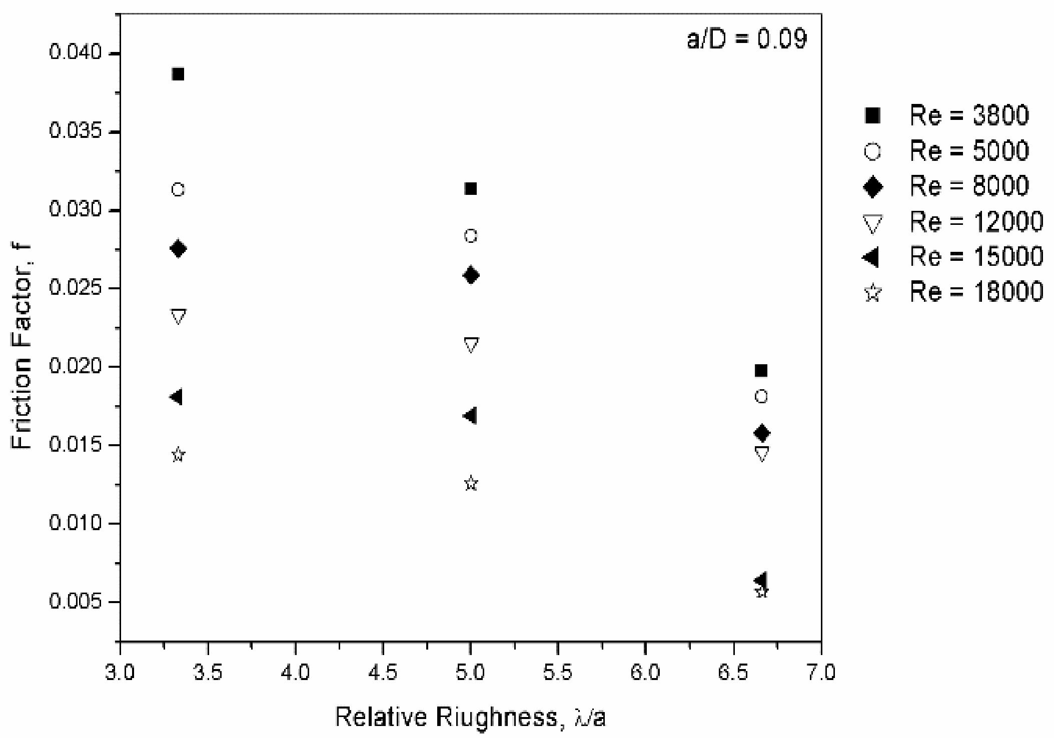

(c)

Fig. 18. “Variation of friction factor as a function of relative roughness wave length (λ/a) for different values of Reynolds number with the (a) Constant a/D = 0.03, (b) Constant” a/D = 0.06, and (c) Constant a/D = 0.09.

ISSN: 2178-7727

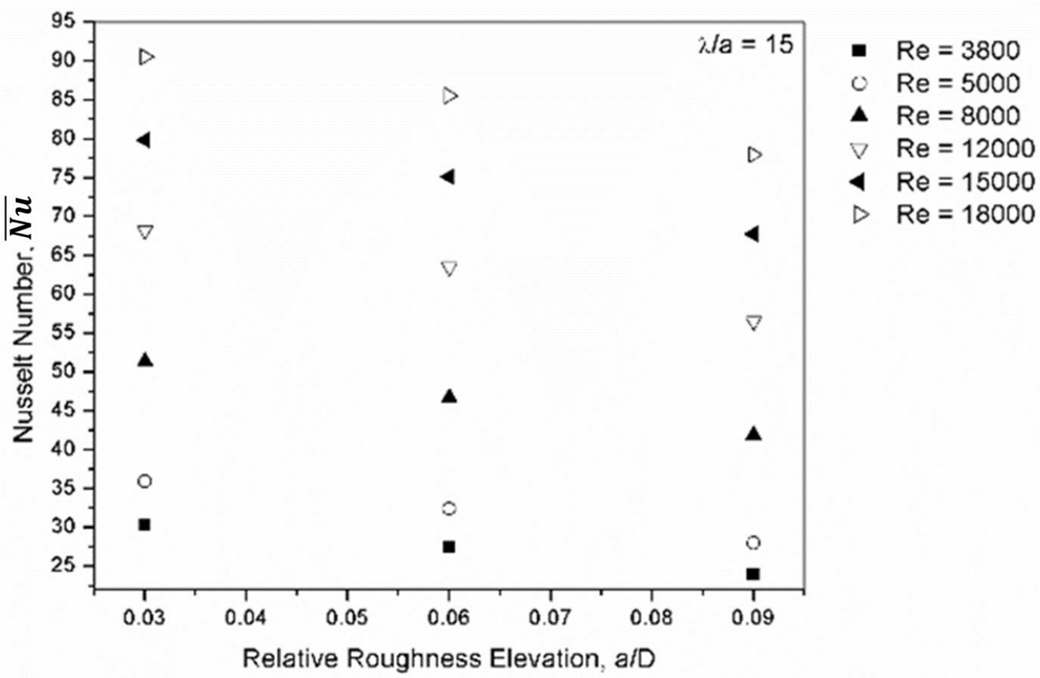

Fig. 19. Variation of the "Nusselt number with the Reynolds number for the different values of a/D at fixed value of" λ/a.

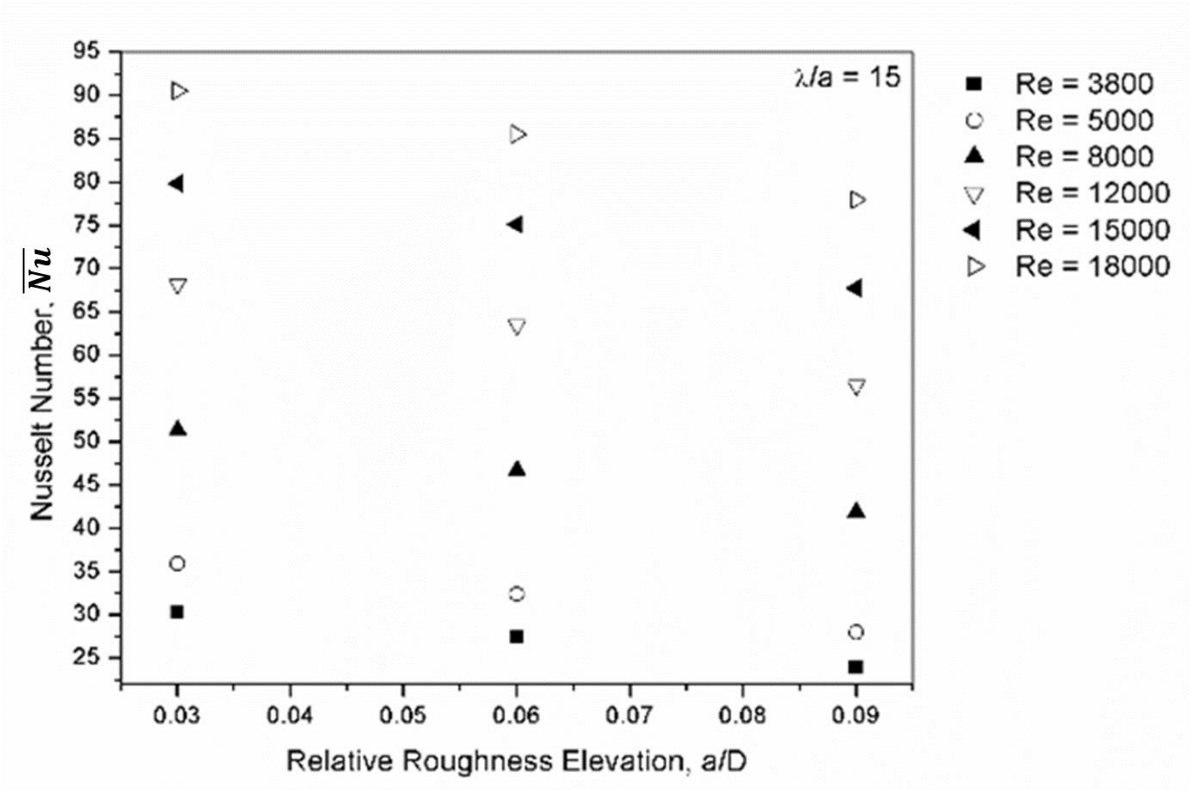

Fig. 20. Variation of "the Nusselt number as a function of relative roughness elevation (a/D) for various values of Reynolds number at fixed value" of λ/a.

ISSN: 2178-7727

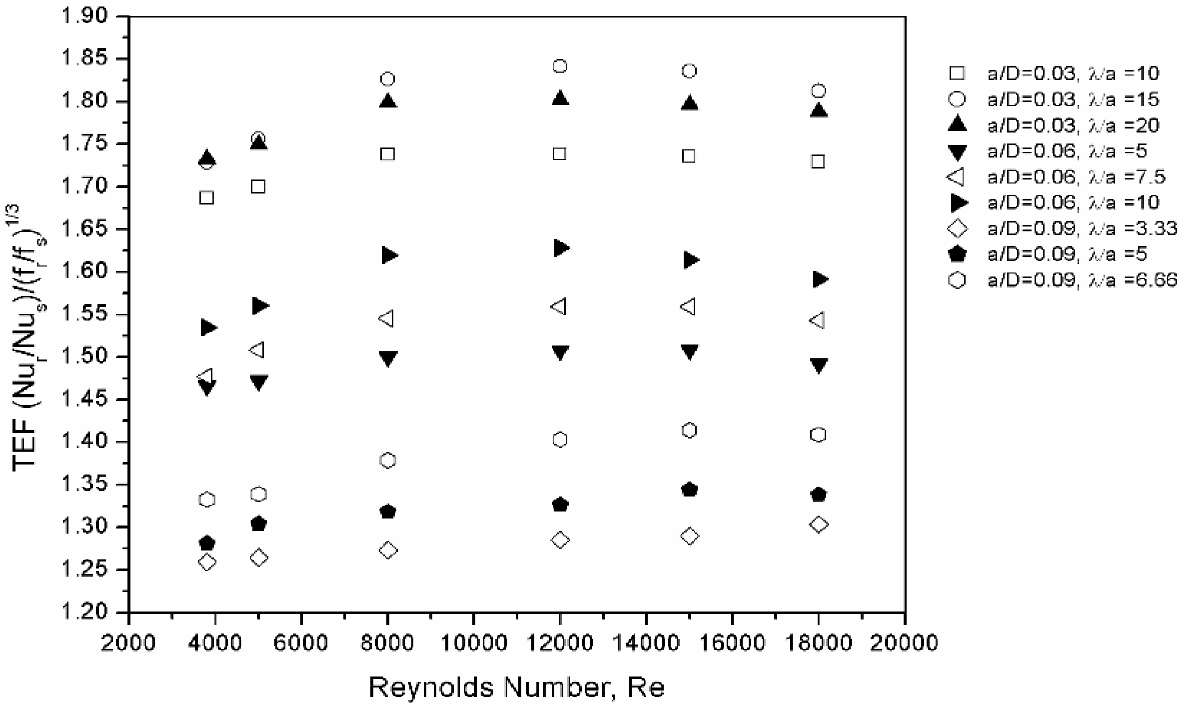

Fig. 21. Variation "of the thermal enhancement factor (TEF) as a function of the Reynolds number for different values of relative roughness elevation (a/D) and relative roughness" wave length (λ/a).

$S_{\text{friction}} \times 10^3$

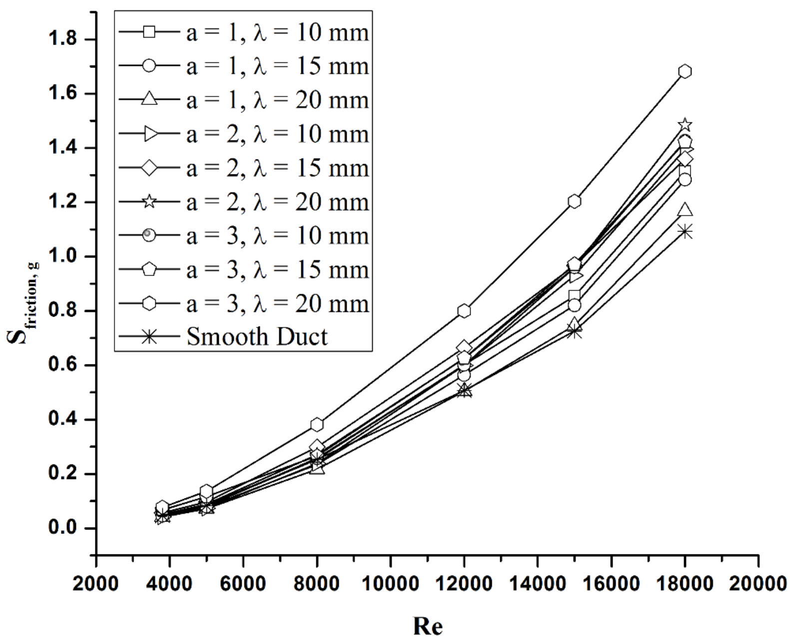

(a)

ISSN: 2178-7727

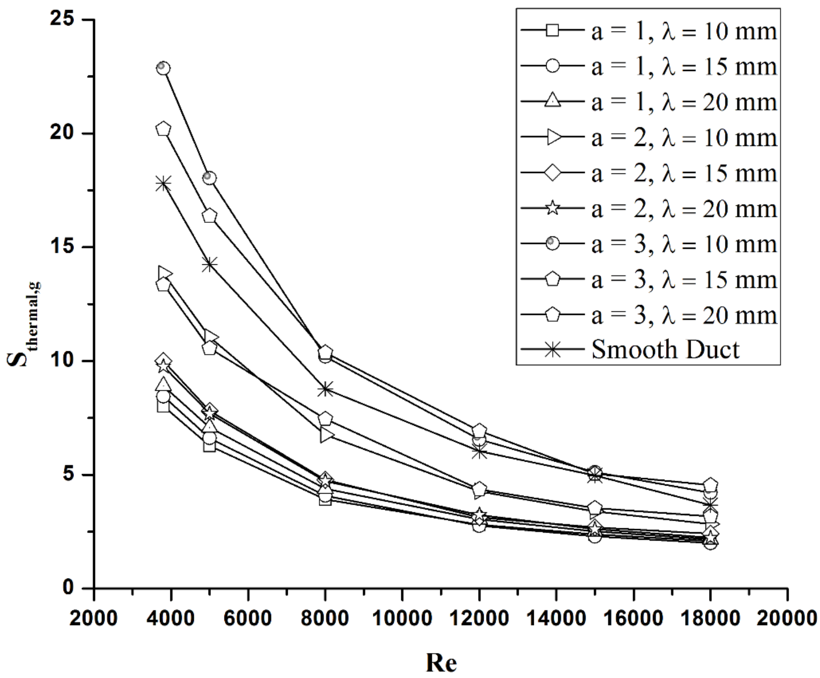

(b)

Fig. 22 Variations of "thermal and frictional entropy generation with Reynolds number.

Table 1.
Thermo-physical properties of air and absorber plate (Aluminum) used in computational work at 27 ºC.

Properties	Working Fluid (Air)	Absorber plate (aluminum)
Density, ρ (kg m^{-3})	1.225	2719
Viscosity, μ (N m^{-2})	1.7894e-05	_
Specific heat, C_p (J $kg^{-1}K^{-1}$)	1006.43	871
Thermal conductivity, k (W m^{-1} k^{-1})	0.0242	202.4

Table 2.
Model design parameters

X1 (mm)	X2 (mm)	X3 (mm)	W (mm)	H (mm)	D (mm)	a (mm)	λ (mm)
225	121	115	100	20	33.33	1, 2, 3	10, 15, 20

Table 3.
Parameter and their range used in computational analysis

Used parameters	Range
Uniform Heat flux, *I*	1000 w/m^2
Prandtl number, Pr	0.7741
Reynolds number, Re	3800-18000 (6 values)
Relative roughness elevation, *a/D*	0.03, 0.06, 0.09
Relative roughness pitch, *λ/a*	3.33-20 (9 values)
Duct aspect" ratio, *W/H*	5

ISSN: 2178-7727

Table 4.
Variation of grid elements and size with Nusselt number and its percentage deviation.

Number of elements	Size of element (mm)	Nusselt number($\overline{Nu}$)	% deviation of $\overline{Nu}$
120000	0.46	65.92	-
154000	0.43	66.60	1.02
164000	0.40	67.50	1.33
174000	0.38	68.38	1.29
184000	0.36	68.50	0.18
192000	0.32	68.54	0.06
196000	0.31	68.55	0.02

Table 5. Heat transfer enhancement ratio for various *a/D* and *λ/a*.

D = 33.33 mm					Nusselt number and friction factor enhancement ratio					
a (mm)	*a/D*	*λ* (mm)	*λ/a*		3800	5000	8000	12000	15000	18000
1	0.03	10	10	Nu_r/Nu_s	1.928205	1.937297	1.978168	1.975862	1.949417	1.888565
				F_r/f_s	1.494075	1.48039	1.47536	1.468595	1.416757	1.302227
		15	15	Nu_r/Nu_s	1.960256	1.965405	1.98626	**1.994253**	1.976214	1.921414
				F_r/f_s	1.458542	1.402076	1.286315	1.270647	1.246745	1.191634
		20	20	Nu_r/Nu_s	1.933333	1.925405	1.919466	1.90977	1.890291	1.838254
				F_r/f_s	1.389735	1.333178	1.214993	1.190562	1.165199	1.085971
2	0.06	10	5	Nu_r/Nu_s	1.588462	1.536216	1.558779	1.602874	1.630583	1.619543
				F_r/f_s	1.272337	1.136052	1.122954	1.202859	1.263332	1.27957
		15	7.5	Nu_r/Nu_s	1.828205	1.855135	1.89542	1.956897	1.925243	1.838254
				F_r/f_s	1.89602	1.860248	1.845297	1.976039	1.882521	1.690864
		20	10	Nu_r/Nu_s	1.857692	1.868108	1.89771	1.913793	1.914563	1.877755
				F_r/f_s	1.772846	1.716711	1.608398	1.623371	1.668566	1.641645
3	0.09	10	3.33	Nu_r/Nu_s	1.321795	1.207568	1.40229	1.347701	1.382524	1.381372
				F_r/f_s	1.15631	1.007106	1.335974	1.152595	1.231363	1.190022
		15	5	Nu_r/Nu_s	1.647436	1.676757	1.687786	1.77931	1.790291	1.75842
				F_r/f_s	2.128032	2.126159	2.099415	**2.415865**	2.363901	2.26872
		20	6.6	Nu_r/Nu_s	1.63205	1.65837	1.71221	1.74712	1.76383	1.72307

ISSN: 2178-7727

6	s	1	8	4	6	5	7
		1.83826	1.89974	1.91516	1.93016	1.94101	1.82860
	F_r/f_s	1	4	2	8	9	5

ISSN: 2178-7727

ACKNOWLEDGEMENTS

The Department of Mechanical Engineering at Chandigarh University, Punjab, supplied the computational resources needed to carry out this simulation investigation employing ANSYS FLUENT. The authors would like to thank the institute for its help in making this research possible and to acknowledge it. This study was not specifically funded by government, business, or nonprofit “entities.

Nomenclature

A_c	surface area of absorber plate, m^2
C_p	specific heat of air, J/kg k
D	equivalent or hydraulic diameter of duct, m
a	wave amplitude, m
h	heat transfer co-efficient, W/m^2 k
H	height of duct, m
I	intensity of solar radiation, W/m^2
k	thermal conductivity of air, W/m k
X	length of duct, m
X_1	entry length of duct, m
X_2	test section length of duct, m
X_3	outlet length of duct, m
$\dot{m}$	mass flow rate, kg/s
ΔP	pressure drop, Pa
λ	wave length, m
T_o	working fluid outlet temperature, K
T_i	working fluid inlet temperature, K
T_a	ambient temperature, K
T_{mp}	average plate temperature, K
T_{am}	average air temperature, K
T_w	wall temperature, K
T_m	bulk mean temperature, K
v	velocity of air through the duct, m/s

Non-dimension parameters

a/D	relative amplitude
f	friction factor
f_r	friction factor for rough duct
f_s	friction factor for smooth duct
$\overline{Nu}$	Nusselt number
Nu_r	Nusselt number for rough surface
Nu_s	Nusselt number for smooth surface
Pr	Prandtl number
λ/a	relative wave length
Re	Reynolds number
W/H	duct aspect ratio

Greek symbols

μ	dynamic viscosity, Ns/m^2
μ_t	turbulent viscosity, Ns/m^2
ρ	density of air, kg/m3
ε	dissipation rate
ω	specific dissipation rate
δ	transition sub-layer thickness, m
k	turbulence kinetic energy, m2/s2

DOI: 10.57030/ASCI.25.4.AS15

ISSN: 2178-7727

Γ molecular thermal diffusivity
Γ_t turbulent thermal diffusivity

Subscripts

am air mean
e ribs height
f fluid (air)
i inlet
m mean
o outlet
pm plate" mean
r roughened
s smooth
t turbulent
w wall

REFERENCES

[1] J.L. Bhagoria, J.S. Saini, S.C. Solanki, Heat transfer coefficient and friction factor correlations for rectangular solar air heater duct having transverse wedge shaped rib roughness on the absorber plate, Renew. Energy. 25 (2002) 341–369.

[2] S.B. Bopche, M.S. Tandale, International Journal of Heat and Mass Transfer Experimental investigations on heat transfer and frictional characteristics of a turbulator roughened solar air heater duct, Int. J. Heat Mass Transf. 52 (2009) 2834–2848.

[3] V.S. Hans, R.P. Saini, J.S. Saini, Heat transfer and friction factor correlations for a solar air heater duct roughened artificially with multiple v-ribs, Sol. Energy. 84 (2010) 898–911.

[4] A. Lanjewar, J.L. Bhagoria, R.M. Sarviya, Heat transfer and friction in solar air heater duct with W-shaped rib roughness on absorber plate, Energy. 36 (2011) 4531–4541.

[5] R. Karwa, G. Chitoshiya, Performance study of solar air heater having v-down discrete ribs on absorber plate, Energy. 55 (2013) 939–955.

[6] N. Singh, S. Chander, J.S. Saini, Performance analysis of solar air heater duct roughened with multigap V-down ribs combined with staggered ribs, Renew. Energy. 91 (2016) 484–500.

[7] V.B. Gawande, Experimental and CFD-based thermal performance prediction of solar air heater provided with right-angle triangular rib as artificial roughness, J. Brazilian Soc. Mech. Sci. Eng. 38 (2016) 551–579.

[8] S. Skullong, P. Promvonge, C. Thianpong, M. Pimsarn, Thermal performance in solar air heater channel with combined wavy-groove and perforated-delta wing vortex generators, Appl. Therm. Eng. 100 (2016) 611–620.

[9] A. Kumar, R. Kumar, R. Maithani, R. Chauhan, M. Sethi, A. Kumari, S. Kumar, S. Kumar, Correlation development for Nusselt number and friction factor of a multiple type V-pattern dimpled obstacles solar air passage, Renew. Energy. 109 (2017) 461–479.

[10] R. Nadda, A. Kumar, R. Maithani, Developing heat transfer and friction loss in an impingement jets solar air heater with multiple arc protrusion obstacles, Sol. Energy. 158 (2017) 117–131.

[11] R. Kumar, R. Chauhan, M. Sethi, A. Kumar, Experimental study and correlation development for Nusselt number and friction factor for discretized broken V-pattern baffle solar air channel, Exp. Therm. Fluid Sci. 81 (2017) 56–75.

[12] S. Kumar, R.P. Saini, CFD based performance analysis of a solar air heater duct provided with artificial roughness, Renew. Energy. 34 (2009) 1285–1291.

[13] S. V Karmare, A.N. Tikekar, Analysis of fluid flow and heat transfer in a rib grit roughened surface solar air heater using CFD, Sol. Energy. 84 (2010) 409–417.

[14] A.S. Yadav, J.L. Bhagoria, A CFD (computational fl uid dynamics) based heat transfer and fl uid fl ow analysis of a solar air heater provided with circular transverse wire rib roughness on the absorber plate, Energy. 55 (2013) 1127–1142.

ISSN: 2178-7727

[15] A. Kumar, M. Kim, ScienceDirect Effect of roughness width ratios in discrete multi V-rib with staggered rib roughness on overall thermal performance of solar air channel, Sol. Energy. 119 (2015) 399–414. doi:10.1016/j.solener.2015.06.030.
[16] T. Alam, M. Kim, Numerical study on thermal hydraulic performance improvement in solar air heater duct with semi ellipse shaped obstacles, Energy. 112 (2016) 588–598.
[17] A. Kumar, M. Kim, Heat transfer and fl uid fl ow characteristics in air duct with various V-pattern rib roughness on the heated plate : A comparative study, Energy. 103 (2016) 75–85.
[18] R. Kumar, A. Kumar, V. Goel, A parametric analysis of rectangular rib roughened triangular duct solar air heater using computational fl uid dynamics, Sol. Energy. 157 (2017) 1095–1107.
[19] R.S. Gill, V.S. Hans, J.S. Saini, S. Singh, Investigation on performance enhancement due to staggered piece in a broken arc rib roughened solar air heater duct, Renew. Energy. 104 (2017) 148–162.
[20] D.S. Thakur, M.K. Khan, M. Pathak, Performance evaluation of solar air heater with novel hyperbolic rib geometry, Renew. Energy. 105 (2017) 786–797.
[21] M.S. Manjunath, K.V. Karanth, N.Y. Sharma, Numerical Investigation on Heat Transfer Enhancement of Solar Air Heater using Sinusoidal Corrugations on Absorber Plate, Int. J. Mech. Sci. Receiv. (2018).
[22] K. Mohammadi, M. Sabzpooshani, Comprehensive performance evaluation and parametric studies of single pass solar air heater with fi ns and baf fl es attached over the absorber plate, Energy. 57 (2013) 741–750.
[23] M.K. Sahu, R.K. Prasad, Exergy based performance evaluation of solar air heater with arc- shaped wire roughened absorber plate, Renew. Energy. 96 (2016) 233–243. doi:10.1016/j.renene.2016.04.083.
[24] R.D. Judkoff, T.P. Mcdowell, S.J. Rees, M.J. Witte, H.M. Newman, C.E. Marriott, D.S. Abramson, K.W. Cooper, A.B. Fraser, R.L. Hall, N.R. Jayaraman, F. Myers, J.C. Peterson, ASHRAE ADDENDA Standard Method of Test for the Evaluation of Building Energy Analysis Computer Programs, (2011).
[25] McAdams WH. Heat transmission. New York: McGraw-Hill; 1942, n.d.
[26] M.A. Fox W, Pritchard P, Introduction to fluid mechanics., John Wiley & Sons;, New York:, 2010.
[27] ANSYS FLUENT. 14.0., Documentation, ANSYS, Inc 2013, n.d.
[28] B. Launder, D. Spalding, Lectures in mathematical models of turbulence., Academic Press;, London, England:, 1972.
[29] S. Patankar, Numerical heat transfer and fluid flow., Washington DC: Hemisphere;, n.d.
[30] R. Webb, RLEckert, Application of rough surface to heat exchanger design., Int. J. Heat Mass Transf. 15(9): (n.d.) 1647–58.
[31] C. Mund, S. K. Rathore, R. K. Sahoo, A review of solar air collectors about various modifications for performance enhancement., Solar Energy. 228 (2021)140-167.
[32] Y. Jiang, H. Zhang, Y. Wang, S. You, Z. Wu, M. Fan, L. Wang, S. Weid, A comparative study on the performance of a novel triangular solar air collector with tilted transparent cover plate., Solar Energy. 227 (2021) 224-235.
[33] E. Alic, M. Das, E. K. Akpinar, Design, manufacturing, numerical analysis and environmental effects of single-pass forced convection solar air collector., Journal of Cleaner Production. 311 (2021) 127518.
[34] M. Ammar, A. Mokni, H. Mhiri, P. Bournot, Numerical analysis of solar air collector provided with rows of rectangular fins., Energy Reports. 6 (2020) 3412-3424.
[35] A. Lingayat, ChandramohanV.P, Numerical investigation on solar air collector and its practical application in the indirect solar dryer for banana chips drying with energy and exergy analysis., Thermal Science and Engineering Progress. 26 (2021) 101077.
[36] H.K. Ghritlahre, M. Verma, J. S. Parihar, D. S. Mondloe, S. Agrawal, A detailed review of various types of solar air heaters performance., Solar Energy (2022) 173-195.
[37] Y. Agrawal, J.L. Bhagoria, A. Gautam, P. K.Chaurasiya, J. A.Dhanraj, J. M.Solomon, S. Salyan, Experimental evaluation of hydrothermal performance of solar air heater with discrete roughened plate, Applied Thermal Engineering. (2022) 118379.
[38] Z. Dong, Q. Du, P. Liu, Z. Liu, W. Liu, A numerical investigation and irreversibility optimization of constantly grooved solar air heaters. Renewable Energy. (2023) 629-646.
[39] R. Karwa, Thermo-hydraulic performance of solar air heater with finned absorber plate forming

ISSN: 2178-7727

multiple rectangular air flow passages in parallel under laminar flow conditions. Applied Thermal Engineering. (2023) 119673.

[40] E. Vengadesan, T. Arunkumar, T. Krishnamoorth, S. Senthil, Thermal performance improvement in solar air heating: An absorber with continuous and discrete tubular and v-corrugated fins. Thermal Science and Engineering Progress. (2024) 102416.